Article

Current Biology

Remodeling the Specificity of an Endosomal CORVET Tether Underlies Formation of Regulated Secretory Vesicles in the Ciliate *Tetrahymena thermophila*

Graphical Abstract

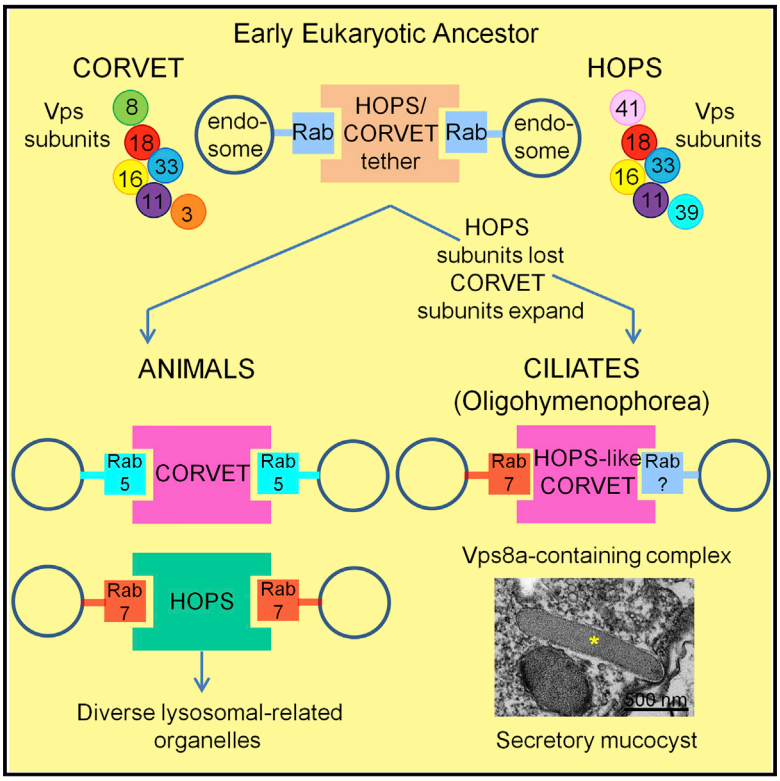

Highlights

- The HOPS complex was lost in a group of ciliates including *Tetrahymena thermophila*
- New CORVET complexes in the same lineage can provide HOPS function
- One CORVET VPS8 paralog is essential for secretory granule formation

Authors

Daniela Sparvoli, Elisabeth Richardson, Hiroko Osakada, ..., Tokuko Haraguchi, Joel B. Dacks, Aaron P. Turkewitz

Correspondence

apturkew@uchicago.edu

In Brief

Sparvoli et al. report a remarkable scenario in eukaryotic membrane trafficking, where lineage-specific loss of a conserved determinant was balanced by expansion and change of specificity in a related complex. This sheds light on the importance of mechanisms associated with lysosome formation in generating elaborate secretory vesicles in eukaryotes.

Sparvoli et al., 2018, Current Biology *28*, 697–710
March 5, 2018
https://doi.org/10.1016/j.cub.2018.01.047

CellPress

Current Biology
Article

Remodeling the Specificity of an Endosomal CORVET Tether Underlies Formation of Regulated Secretory Vesicles in the Ciliate *Tetrahymena thermophila*

Daniela Sparvoli,[1] Elisabeth Richardson,[2,10] Hiroko Osakada,[3,10] Xun Lan,[4,5,10] Masaaki Iwamoto,[3] Grant R. Bowman,[1,11] Cassandra Kontur,[1,12] William A. Bourland,[6] Denis H. Lynn,[7,13] Jonathan K. Pritchard,[4,5,8] Tokuko Haraguchi,[3,9] Joel B. Dacks,[2] and Aaron P. Turkewitz[1,14,*]

[1]Department of Molecular Genetics and Cell Biology, The University of Chicago, Chicago, IL, USA
[2]Department of Cell Biology, University of Alberta, Edmonton, AB T6G 2R3, Canada
[3]Advanced ICT Research Institute, National Institute of Information and Communications Technology (NICT), Kobe 651-2492, Japan
[4]Department of Genetics, Stanford University, Stanford, CA 94305, USA
[5]Howard Hughes Medical Institute, Stanford University, Stanford, CA 94305, USA
[6]Department of Biological Sciences, Boise State University, Boise, ID 83725-1515, USA
[7]Department of Integrative Biology, University of Guelph, Guelph, ON N1G 2W1, Canada
[8]Department of Biology, Stanford University, Stanford, CA 94305, USA
[9]Graduate School of Frontier Biosciences, Osaka University, Suita 565-0871, Japan
[10]These authors contributed equally
[11]Present address: Department of Molecular Biology, University of Wyoming, Laramie, WY, USA
[12]Present address: Department of Genetics, Yale University School of Medicine, New Haven, CT 06510, USA
[13]Present address: Department of Zoology, University of British Columbia, Vancouver, BC V6T 1Z4, Canada
[14]Lead Contact
*Correspondence: apturkew@uchicago.edu
https://doi.org/10.1016/j.cub.2018.01.047

SUMMARY

In the endocytic pathway of animals, two related complexes, called CORVET (class C core vacuole/endosome transport) and HOPS (homotypic fusion and protein sorting), act as both tethers and fusion factors for early and late endosomes, respectively. Mutations in CORVET or HOPS lead to trafficking defects and contribute to human disease, including immune dysfunction. HOPS and CORVET are conserved throughout eukaryotes, but remarkably, in the ciliate *Tetrahymena thermophila*, the HOPS-specific subunits are absent, while CORVET-specific subunits have proliferated. VPS8 (vacuolar protein sorting), a CORVET subunit, expanded to 6 paralogs in *Tetrahymena*. This expansion correlated with loss of HOPS within a ciliate subgroup, including the Oligohymenophorea, which contains *Tetrahymena*. As uncovered via forward genetics, a single *VPS8* paralog in *Tetrahymena* (*VPS8A*) is required to synthesize prominent secretory granules called mucocysts. More specifically, *Δvps8a* cells fail to deliver a subset of cargo proteins to developing mucocysts, instead accumulating that cargo in vesicles also bearing the mucocyst-sorting receptor Sor4p. Surprisingly, although this transport step relies on CORVET, it does not appear to involve early endosomes. Instead, *Vps8a* associates with the late endosomal/lysosomal marker Rab7, indicating that target specificity switching occurred in CORVET subunits during the evolution of ciliates. Mucocysts belong to a markedly diverse and understudied class of protist secretory organelles called extrusomes. Our results underscore that biogenesis of mucocysts depends on endolysosomal trafficking, revealing parallels with invasive organelles in apicomplexan parasites and suggesting that a wide array of secretory adaptations in protists, like in animals, depend on mechanisms related to lysosome biogenesis.

INTRODUCTION

Cells devote enormous resources to interact with and modify their surroundings. One cellular strategy is to externalize proteins, either by expressing them on the cell surface or by secreting them. Proteins to be secreted are first translocated from the cytoplasm into the endoplasmic reticulum, from where they are transported through successive membrane-bound compartments and, finally, into vesicles [1, 2]. When vesicles fuse with the plasma membrane, called exocytosis, the proteins in the vesicle membrane are exposed on the cell surface while vesicle contents are secreted. In regulated exocytosis, the final exocytic event occurs in response to extracellular stimuli [3, 4].

In animal tissues, multiple classes of vesicles undergo regulated exocytosis to release peptides and other molecules that facilitate fluent cell-cell communication. Dense core granules, such as those in which endocrine hormones are stored for regulated release, arise from the *trans*-Golgi [5, 6]. A second class of vesicles, which store diverse cargos in different tissues, are called LROs (lysosome-related organelles) [7]. In humans, LROs are vital structures, including melanosomes,

Weibel-Palade bodies, and T cell lytic granules [8]. LRO formation depends on trafficking from the *trans*-Golgi, but LROs simultaneously receive cargo from endosomes [9, 10]. LRO formation involves cytoplasmic and membrane proteins, including the small GTPases Rab32/38, SNAREs (soluble NSF attachment protein receptor), the AP3 coat adaptor complex, and a sorting receptor, sortilin/VPS10 [11–15]. LRO formation also involves the HOPS complex, a 6-subunit heterohexamer that functions as a multivalent tether between endosomal compartments to facilitate their subsequent fusion [16, 17]. Four HOPS (homotypic fusion and protein sorting) subunits (VPS11, 16, 18, and 33) are also found in a related complex, CORVET (Class C core vacuole/endosome transport), while the remaining 2 subunits in each complex are complex specific [18, 19]. As shown primarily in budding yeast and animals, CORVET and HOPS are also functionally related, acting as tethers at Rab5- and Rab7-positive endosomes, respectively [20–22]. In mammalian cells, these correspond to successive stages in endosome maturation [23].

Pathways involved in endosomal trafficking and lysosome formation appear to have been present at the time of the last eukaryotic common ancestor (LECA) [24–27]. LECA was a unicellular organism that existed ~1.5 billion years ago, whose membrane compartments have been inferred based on morphological comparisons and genomics-based surveys of compartmental determinants in its descendants, the extant eukaryotes [28] (inter alia). Another inference from such surveys is that many lineages, in addition to animals, have evolved increasingly complex secretory pathways, but the cell biological details are largely underexplored. Based on microscopy, secretory vesicles in the Alveolate protists, collectively called extrusomes, attracted notice due to their large size, regulated exocytosis, and often elaborate morphologies [29–31]. The Alveolates include largely free-living ciliates and dinoflagellates and parasitic apicomplexans. Extrusomes in ciliates are functionally and compositionally distinct from those in apicomplexans: the former are used for predation or defense, and perhaps for encystment, while the latter are deployed during host cell invasion [31–36]. However, accumulating evidence indicates that extrusome formation in both ciliates and apicomplexans involves genes associated with LRO biogenesis.

The best-studied apicomplexan extrusomes are the rhoptries in the globally important parasites *Toxoplasma gondii* and *Plasmodium falciparum* [36]. Rhoptries were initially linked with LROs based on morphological considerations, since they contain internal membranes and, thus, resemble endosomal multivesicular bodies in animal cells [37]. This idea received molecular support from recent studies in apicomplexans demonstrating the involvement of a VPS10/sortilin receptor, early endocytic Rab GTPases, and the VPS11 subunit of the HOPS/CORVET complex [38–41].

Ciliates are an impressively diverse and ecologically important group of microbes, found in nearly all freshwater, marine, and terrestrial environments [42]. The best-studied ciliate extrusomes are trichocysts in *Paramecium tetraurelia* and mucocysts in *Tetrahymena thermophila*. The mucocyst lumen is primarily filled with densely packed Granule lattice (GRL) proteins, which are delivered to immature mucocysts as proproteins and then undergo proteolytic maturation by aspartyl- and cysteine-cathepsins Cth3p and Cth4p [43, 44]. Processing is essential for secretion, because only processed Grl proteins can form a matrix that expands upon exocytosis to extrude the mucocyst contents. A second family of proteins in mucocysts is called GRT/IGR (Granule tip/Induced on Granule Regeneration) [45, 46]. Significantly, mucocysts are not multivesicular, unlike Apicomplexan rhoptries. However, the delivery to mucocysts of Cth3p and Grt/Igr proteins, but not the Grl proteins, requires the sortilin/VPS10 receptor Sor4p, as well as an endosomal SNARE, Stx7l1p (Syntaxin 7-like) [47, 48]. A key finding was that *Δstx7l1* cells accumulate cytoplasmic non-docked vesicles that contain condensed cores of Grl proteins in the unprocessed form. Importantly, those vesicles do not contain the set of mucocyst proteins that depend on Sor4p for their delivery in wild-type cells, suggesting that Stx7l1p is required for just one of two pathways for mucocyst cargo delivery. These results suggested that extrusomes in ciliates may depend on LRO-related mechanisms that bear fundamental similarities with those used in apicomplexans. The relationship could be clarified by understanding the role of endosomal tethers in ciliate extrusome formation. Intriguingly, though the HOPS complex is broadly conserved throughout eukaryotes, the HOPS-specific subunits VPS39 and 41 are absent in *Tetrahymena* and were also lost independently in some apicomplexans [49].

One approach to analyzing mucocyst biogenesis is isolating chemically induced mutants, followed by whole-genome sequencing to pinpoint the causative lesions [50]. In this work, we investigate UC616, a mutant previously isolated as part of a large screen [46], and, thereby, we uncover direct evidence for an endosomal intermediate in mucocyst biogenesis. Our data indicate that, in *Tetrahymena*, a novel CORVET paralog provides HOPS-like function. Our phylogenetic analysis maps the loss of HOPS in *Tetrahymena* and related Oligohymenophorean ciliates, balanced by an expansion of paralogs in CORVET-specific genes. With these new results, a comparison of regulated secretion in apicomplexans and ciliates indicates that broadly similar mechanisms, evolved in parallel, were employed to generate two dramatically different, highly complex secretory compartments.

RESULTS

UC616 Bears a Recessive Mutation that Blocks Mucocyst Formation

The *Tetrahymena* mutant strain UC616 failed to release mucocyst contents upon stimulation (Figure S1A). The defect was at the level of mucocyst formation, as judged by the failure of proGrl proteins to undergo proteolytic maturation (Figure S1B). In addition, both GRL and GRT proteins were localized aberrantly in UC616 (Figure 1A, second panel). Electron microscopy (EM) analysis revealed small electron-dense structures in the cytoplasm of the mutant cells, distinct from wild-type mucocysts (Figure 1B). These structures were similar in appearance (Figures S1C and S1D) and size (Figure S1E) to Grl3p-containing mucocyst intermediates in the *Δstx7l1* mutant, which is defective in homotypic and/or heterotypic fusion required for mucocyst formation [48]. In standard genetic crosses, all defects in UC616 segregated as expected for a single recessive Mendelian mutation (data not shown). Other matings revealed that UC616 was allelic to SB281, a previously described mutant in mucocyst

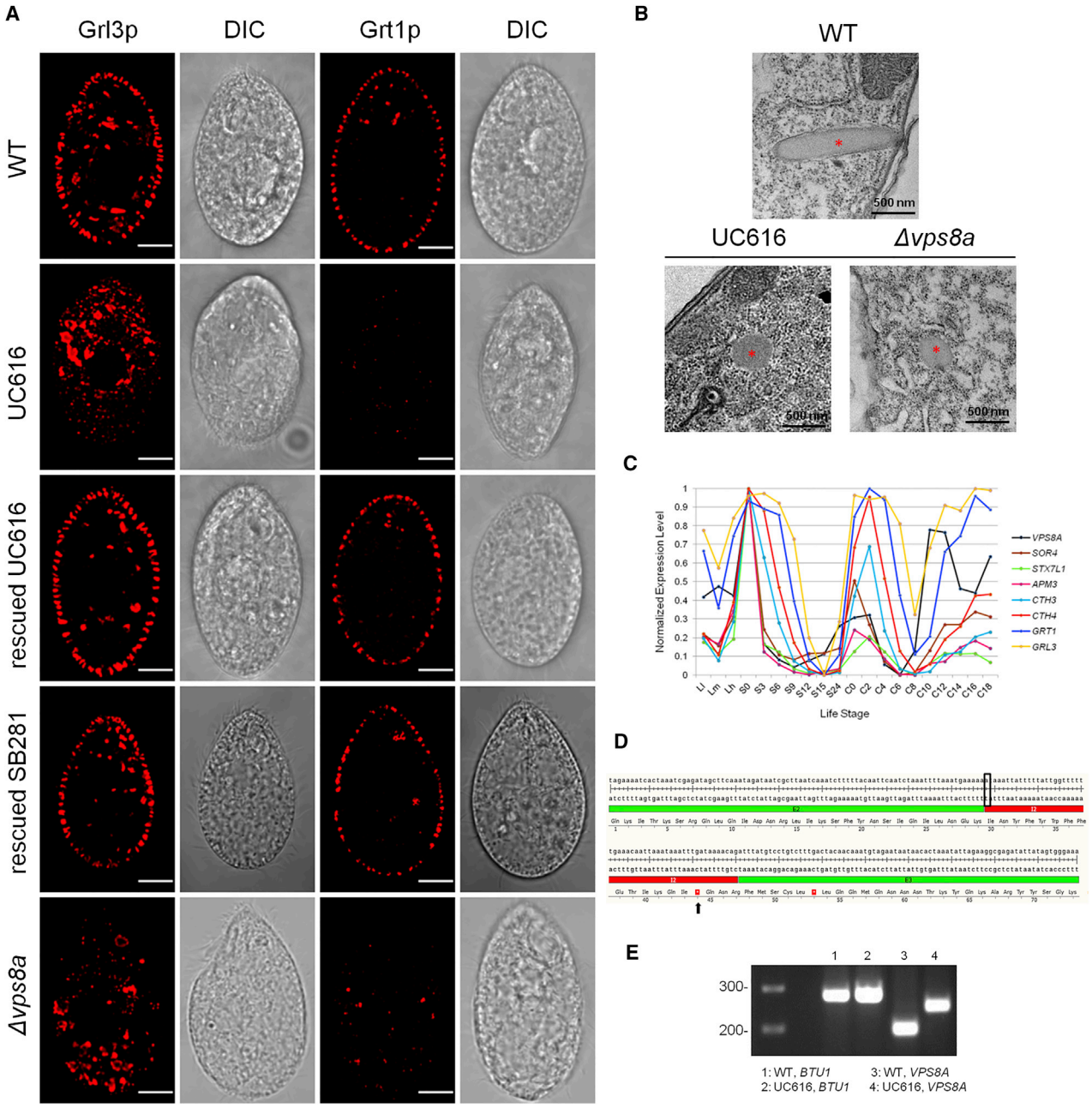

Figure 1. Vps8a Is Essential for Mucocyst Biogenesis

(A) Confocal cross sections, with paired differential interference contrast (DIC) images, of wild-type, UC616, rescued UC616 and SB281, and *Δvps8a*. Cells were immunostained with mAbs 5E9 and 4D11, which recognize mucocyst proteins Grl3p (left) and Grt1p (right), respectively. The wild-type pattern of docked mucocysts is absent in UC616 and *Δvps8a*, but it was restored in UC616 and SB281 expressing a *VPS8A*-GFP transgene. Scale bars, 10 μm.

(B) Electron microscopy. In wild-type, mucocysts dock at the plasma membrane. In contrast, UC616 and *Δvps8a* contain cytoplasmic vesicles with granular cores (labeled with asterisks). Scale bars, 500 nm.

(C) The expression profile of *VPS8A* (black line) is similar to that of mucocyst-related genes *SOR4*, *STX7L1*, *APM3*, *CTH3*, *CTH4*, *GRT1*, and *GRL3*. For the plot, based on data downloaded from http://tfgd.ihb.ac.cn, each value was normalized to that gene's maximum expression level. The conditions sampled were growing cultures (low Ll, medium Lm, and high Lh culture density), starvation over 24 hr (S0–S24), and time points during conjugation (C0–C18).

(D) Alignment of the *VPS8A* exon(E2)-intron(I2) junction, and the corresponding translated sequence. The G/A-C/T mutation (black box) results in a premature stop codon (black arrow) 41 bp downstream.

(E) Intron 2 is retained in the *VPS8A* transcript in UC616. Columns 1 and 2 correspond to wild-type and UC616 cDNA that was PCR-amplified with *BTU1* primers as control; in lanes 3 and 4, the primers flanked intron 2 in *VPS8A*. 2% ethidium bromide-stained gel, with 200- and 300-bp DNA fragments are indicated to the left.

See also Figure S1.

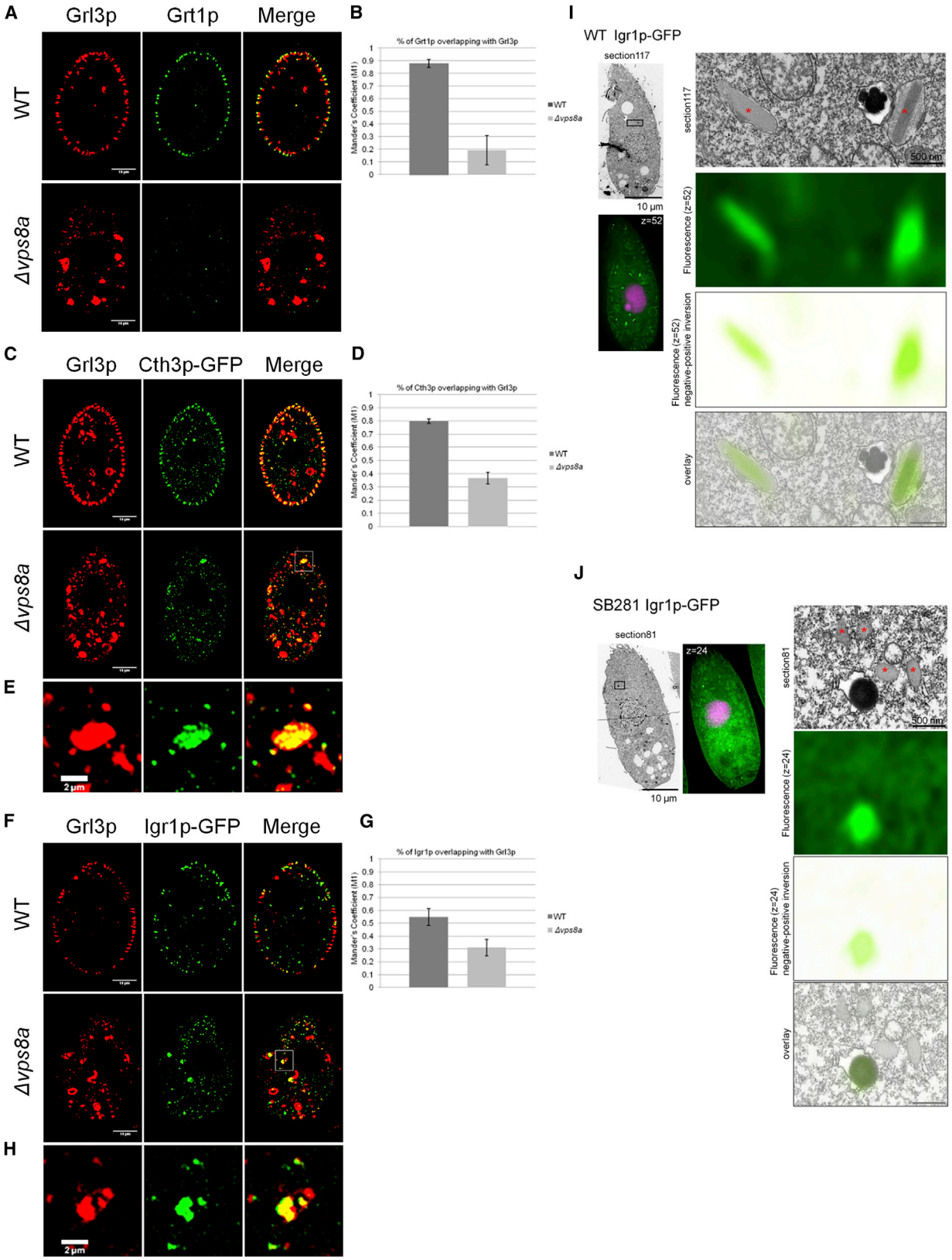

Figure 2. Multiple Mucocyst Proteins Are Not Delivered to Mucocyst Intermediates in *Δvps8a* Cells

(A) Wild-type (upper panel) and *Δvps8a* (bottom panel) cells, co-stained with anti-Grl3p (5E9) and anti-Grt1p (4D11) mAbs conjugated with AlexaFluor 650 and AlexaFluor 488 dyes, respectively. Co-localization between Grt1p and Grl3p is markedly reduced in *Δvps8a*. Confocal cross sections are shown for clarity. Scale bars, 10 μm.

(legend continued on next page)

biogenesis [51, 52] (i.e., all UC616 × SB281 were fully mutant; data not shown).

Sequencing Pools of UC616 Progeny Identify Causative Mutation in the *VPS8A* Gene

We outcrossed and backcrossed UC616 to obtain progeny, from which we picked single cells that were subsequently expanded to clones. We determined each clone's phenotype as either mutant or wild-type for regulated exocytosis. Since the mutation is recessive, the mutant allele should be homozygous in the first group of clones but heterozygous or absent in the latter (Figure S1F). Clones from each category were pooled and their whole genomes sequenced. Single-nucleotide variants (SNVs) were then identified that were homozygous only in the mutant pool. Ten such SNVs fell within predicted genes. One of these genes, which we named *VPS8A*, had an expression profile (downloaded from the Tetrahymena Functional Genomics Database [TFGD]; http://tfgd.ihb.ac.cn/) that is shared with many factors involved in mucocyst biogenesis (Figure 1C) [53]. *VPS8A* is a homolog of pan-eukaryotic VPS8, which encodes one of the two CORVET-specific subunits, i.e., not shared with HOPS [54]. *VPS8A* in UC616 bears a G-to-A mutation predicted to interfere with intron excision (Figures 1D and S1G). We confirmed that intron 576957–577009 (on the reverse strand) was aberrantly retained in UC616 (Figure 1E). This introduced a stop codon 42 nt downstream the splice junction (Figure 1D), resulting in the truncation of the 1,499-residue wild-type protein at residue 522, followed by 14 additional novel residues. Surprisingly, genome sequencing of the SB281 mutant identified the identical splice site mutation, while the uniqueness of background SNVs in the two mutant strains confirmed that they were unrelated (data not shown).

Both UC616 and SB281 accumulated full cohorts of docked mucocysts after we introduced a wild-type copy of *VPS8A* (Figure S1H; Figure 1A, panels 3 and 4). Such cells were also rescued with regard to proGrl proteolytic processing and exocytosis competence (Figures S1I and S1J). Moreover, the UC616 phenotypes were reproduced when we disrupted all copies of the Macronuclear *VPS8A* gene (Figure S1K) (Figure 1A, fifth panel; Figures S1I and S1J). *VPS8A* is, therefore, the locus of the causative mutation in UC616 and SB281, and it is required for mucocyst biogenesis. The gene is non-essential and knockout cells (*Δvps8a)* had no growth defect (doubling times: wild-type [WT], 2.6 hr; *Δvps8a*, 2.3 hr).

VPS8A Is Required for Efficient Delivery of a Subset of Mucocyst Proteins

Previous work indicated that pro-Grl proteins appear to be mistargeted in SB281 [46, 52]. We expanded this analysis in the better-defined *Δvps8a* strain, while also taking advantage of recently described mucocyst components. Specifically, we imaged endogenous Grl3p in pairwise combination with four non-GRL proteins that localize to mucocysts. Three of these (Grt1p, Igr1p, and Cth3p) are soluble proteins in the mucocyst lumen, while the fourth is a membrane-associated SNARE, Stx7l1p. GFP-tagged Stx7l1p co-localized equally with Grl3p in both wild-type and mutant cells, indicating that its targeting does not depend on *VPS8A* (Figures S2A and S2B). In contrast, co-localizations of Grt1p and Cth3p (tagged with GFP at the endogenous locus) with endogenous Grl3p were reduced by 78% and 54%, respectively, in *Δvps8a* compared to wild-type (Figures 2A–2D).

A third lumenal protein, Igr1p (Induced during granule regeneration), was overexpressed as a GFP-tagged copy. Igr1p-GFP showed ~40% reduced co-localization with Grl3p in the mutant compared to wild-type (Figures 2F and 2G). Significantly, the transport of Grt1p, Igr1p, and Cth3p all depend on Sor4p [47]. Given the known role of CORVET in other organisms in promoting specific endosomal fusion, we therefore hypothesized that Vps8a acts during mucocyst biogenesis to promote heterotypic fusion between a Sor4p-containing compartment and a Grl-containing compartment (Figure 3).

For Cth3p-GFP and Igr1p-GFP, the co-localization with Grl3p that persisted in *Δvps8a* appeared due in large part to inclusion in large structures (Figures 2E and 2H), distinct from the ~0.4-μm spherical vesicles noted earlier (Figures S1C–S1E). These relatively large compartments were likely to be degradative rather than biosynthetic, based on correlative light and electron microscopy analysis of the Igr1p-GFP-expressing cells (Figures 2I and 2J) and on co-localization with LysoTracker (Figures S2C and S2D). There was also increased co-localization between Grl3p (expressed as Grl3p-GFP; Figure S2E) with LysoTracker in the *Δvps8a* cells compared to wild-type (Figures S2F and S2G).

(B) Percentage of overlap between Grt1p and Grl3p (Mander's coefficient M1) was calculated with 25 non-overlapping images/sample using Fiji-JACoP plugin. Error bars represent SDs.

(C) Localization of Cth3p-GFP in wild-type and *Δvps8a* cells. Cells were immunolabeled with 5E9 anti-Grl3p and rabbit anti-GFP antibodies. Co-localization of Cth3p-GFP with Grl3p is reduced in *Δvps8a*, and the proteins localize in heterogeneous cytoplasmic vesicles.

(D) Overlap between Cth3p-GFP and Grl3p was calculated as in (B), based on 40 non-overlapping images/sample. Error bars represent SDs.

(E) Magnification of the boxed area in (C) (merge), showing co-localization of Cth3p-GFP and Grl3p in a large compartment in *Δvps8a*.

(F) Localization of Igr1p-GFP in wild-type and *Δvps8a* cells. Cells were immunolabeled with mAb 5E9. Co-localization of Igr1p-GFP with Grl3p is reduced in *Δvps8a*.

(G) Overlap between Igr1p-GFP and Grl3p was calculated as in (B), based on 25 non-overlapping images/sample. Error bars represent SDs.

(H) Magnification of the boxed area in (F) (merge), showing co-localization of Igr1p-GFP and Grl3p in a large compartment in *Δvps8a*.

(I and J) Correlative light electron microscopy (CLEM) imaging of overexpressed Igr1p-GFP in wild-type (I) and mutant (SB281, which bears the identical *VPS8A* mutation as UC616) (J). Fluorescence images (lower images) are paired with the corresponding electron micrographs (upper images). Left, low magnification images. Scale bar, 10 μm. The fuschia-stained structures are the Micro- and Macronuclei stained with DAPI; green represents Igr1p-GFP. Right, boxed regions in the left images are shown at high magnification. From top to bottom: EM image, fluorescence image (Igr1p-GFP), fluorescence image inverted (negative to positive) and then overlaid on the electron micrograph to show precise mapping of the fluorescence signals onto cellular structures. In wild-type, Igr1p-GFP is present in mucocysts. In SB281, Igr1p-GFP does not accumulate in the granular mucocyst-related vesicles (asterisks), but it is instead found in electron-dense structures likely to represent degradative compartments. Scale bar, 0.5 μm.

See also Figure S2.

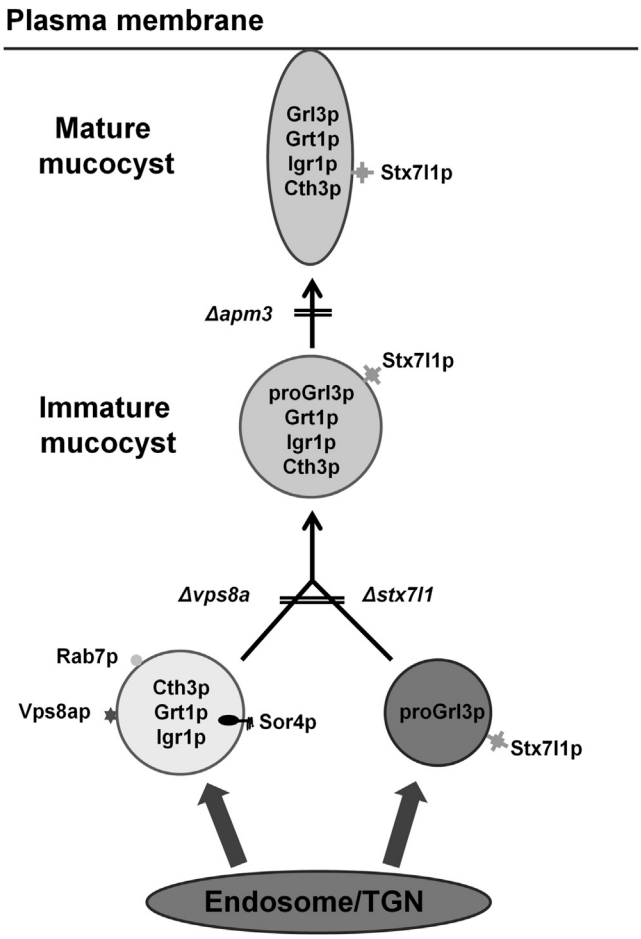

Figure 3. Model for Mucocyst Biogenesis in *Tetrahymena thermophila*

Two different types of vesicles deliver cargo to immature mucocysts. The first is generated directly from a *trans*-Golgi compartment and contains condensed proGrl proteins. These vesicles accumulate in both *Δstx7l1* and *Δvps8a* mutants; similar vesicles, though docked at the plasma membrane, accumulate in *Δsor4*. The second corresponds to a late endosomal compartment, and it transports the protease Cth3p and members of the GRT family, Grt1p and Igr1p, bound to the sorting receptor Sor4p. For simplicity, we depict a single compartment that functions both as a *trans*-Golgi and an early endosome, as has been described in plants [55]; whether these are separate compartments in ciliates is unknown. The CORVET subunit Vps8ap (this paper) and the mucocyst-resident syntaxin Stx7l1p mediate the tethering and fusion between the two classes of vesicles. The AP-3 complex (*APM3*: μ subunit) appears required for delivery of some as-yet unidentified mucocyst maturation factors.

These results suggest that diverse abortive mucocyst intermediates in *Δvps8a* are targeted for degradation.

Δvps8a Cells Accumulate Vesicles Containing Mis-targeted Luminal Proteins and Their Sorting Receptor

The mis-targeting of Grt1p, Igr1p, and Cth3p in *Δvps8a* can be explained if vesicles containing Sor4p and its bound ligands fail to be delivered to immature mucocysts, so we sought direct evidence for their existence. In wild-type cells, GFP-tagged Sor4p, expressed from the endogenous locus, localized to small mobile cytoplasmic vesicles [47]. Although Sor4p shows robust biochemical interaction with Grt1p and is absolutely required for its delivery to mucocysts [47], the two proteins in wild-type cells showed no significant co-localization (Figures 4A and 4B). In contrast, Sor4p and Grt1p in *Δvps8a* cells co-localized extensively (Figures 4A and 4B) in vesicles whose size distribution was somewhat shifted compared with Sor4p-containing vesicles in wild-type cells (Figure 4C). The altered localization of Sor4p-GFP in *Δvps8a* did not reflect targeting to degradative compartments, since the puncta did not label with LysoTracker (Figures S3A and S3B), and Sor4p-GFP in such cells accumulated to higher than wild-type levels (Figure 4D). These puncta may represent transport intermediates that are transient in wild-type cells but trapped in *Δvps8a* because they are blocked in fusion with their acceptor compartment. They appeared to derive from endosomes, as suggested by the 2.7-fold and 5.1-fold increased co-localization of the endocytic tracer FM4-64 with Sor4p-GFP or Igr1p-GFP, respectively, in *Δvps8a* compared to wild-type (Figures 4E, 4F, S3C, and S3D). Importantly, in the *Δvps8a* cells, Sor4p-GFP showed no significant co-localization with Grl3p (Figures S3E and S3F), consistent with the idea that Grl proteins are delivered to mucocysts via a different route from Sor4p cargo. Taken together, these results support the model in Figure 3.

VPS8 Underwent Paralogous Expansion and Functional Diversification in the Ciliate Lineage Containing *T. thermophila*

VPS8 is represented by a single gene in *H. sapiens*, *S. cerevisiae*, *D. melanogaster*, *T. gondii*, and many other eukaryotes. In contrast, six *VPS8* paralogs exist in *T. thermophila*. Our phylogenetic analysis showed that at least four paralogs were maintained since the ancestor of the Oligohymenophorean ciliate lineage (Figure S4A). The root of the tree was determined using *Oxytricha trifallax* Vps8 sequences as an outgroup, and the monophyly of the Oligohymenophorea-containing clade to the exclusion of Oxytricha had complete support under both MrBayes and RAxML (1/100). This analysis indicates that the post-Spirotrichea expansions occurred independently of expansions in other lineages, and it led us to postulate distinct functional roles for individual VPS8 paralogs that arose in Oligohymenophorea. Consistent with this idea, the six *T. thermophila* paralogs have non-identical expression profiles (Figure 5A), and the *VPS8A* profile appears unique. To test whether functional diversification had occurred between paralogs, we targeted each of the additional five paralogs for knockout in the Macronucleus. For two of the genes, we could not recover viable knockout cells, i.e., a drug resistance cassette integrated at the Macronuclear locus could not be driven to fixation (Figure S4B). The results indicate that two paralogs are essential under these culture conditions, unlike *VPS8A*. Targeted disruption of the remaining three paralogs revealed that complete loss of *VPS8B*, *E*, or *F* had no effect on mucocyst secretion (Figures 5B and S4C). Thus, *VPS8A* represents a CORVET subunit that appears specialized for a single pathway of endolysosomal trafficking, and it may have little functional overlap with other *VPS8* paralogs. Labeling of the *Δvps8b*, *Δvps8e*, and *Δvps8f* cells with FM4-64 suggests that Vps8b and Vps8e may be involved in phagolysosome maturation (Figures S4D and S4E).

As tethers, CORVET complexes bridge two membranes by interacting with RabGTPases and SNAREs on the target

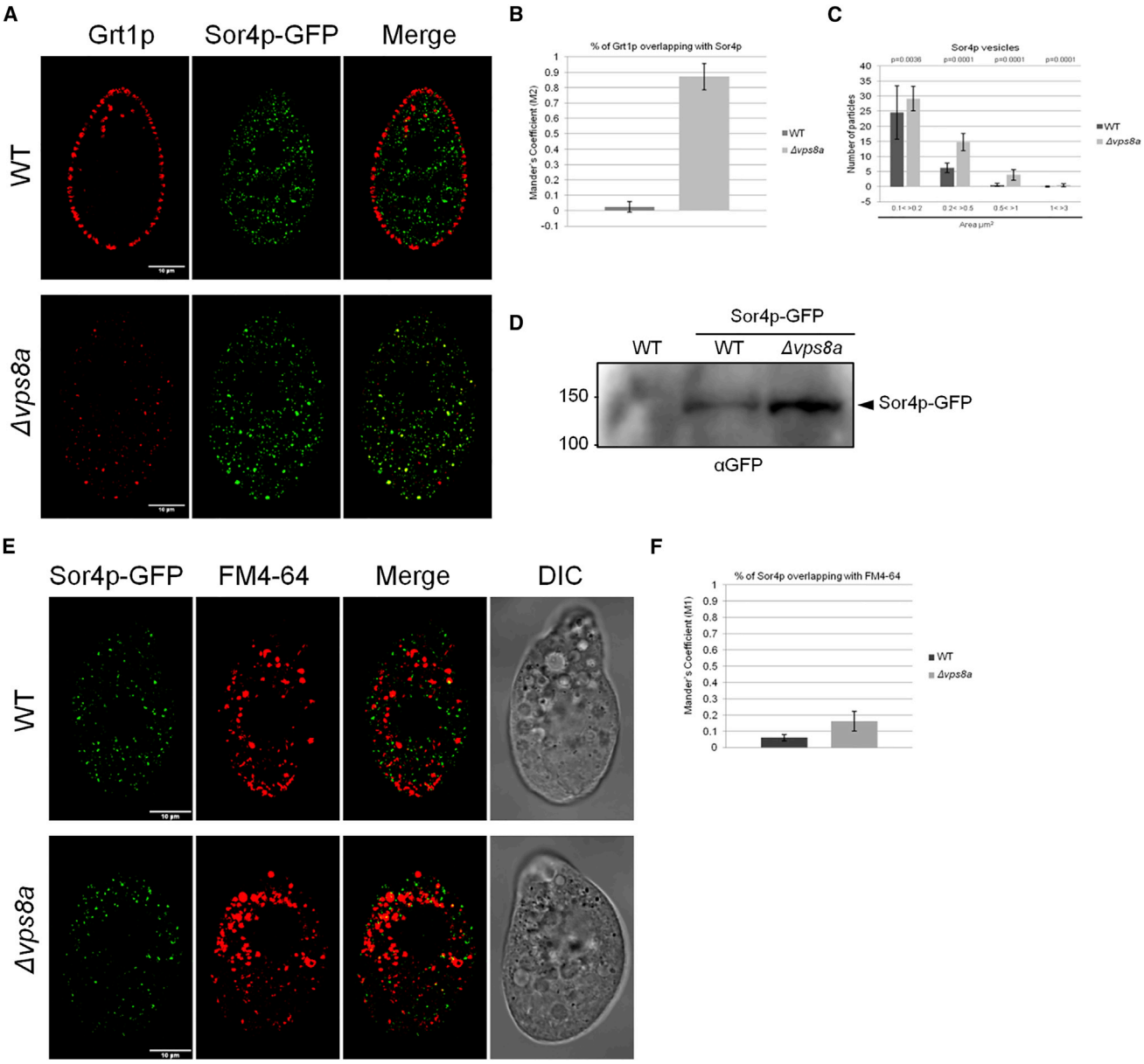

Figure 4. Sor4p Co-localizes with Its Ligand Grt1p in *Δvps8a*, but Not Wild-Type, Cells

(A) Wild-type and *Δvps8a* expressing Sor4p-GFP were immunolabeled with anti-Grt1p mAb. Confocal cross sections are shown for clarity. Scale bars, 10 μm.

(B) Overlap between Grt1p and Sor4p-GFP (M2) was calculated as in Figure 2B, based on 40 non-overlapping images/sample. Error bars represent SDs.

(C) The distribution of Sor4p-GFP vesicle sizes is shifted in *Δvps8a* compared to wild-type. Shown are mean particle counts and SDs (error bars) for each size class, calculated using the Fiji tool Analyze Particles, with 40 non-overlapping images/sample. The p values were determined by two-tailed t test. There are significant increases in vesicle number in *Δvps8a* compared to wild-type in multiple size classes: ($0.1 < > 0.2\ \mu m^2$) = 0.6-fold; ($0.2 < > 0.5\ \mu m^2$) = 1.6-fold; ($0.5 < > 1\ \mu m^2$) = 5.8-fold. In addition, rare Sor4p-GFP-positive structures of ($1 < > 3\ \mu m^2$) appear almost exclusively in *Δvps8a*.

(D) SDS-PAGE and western blotting of whole-cell lysates from 1.5×10^5 wild-type and *Δvps8a* cells expressing Sor4p-GFP, and an untransformed wild-type control, probed with anti-GFP antibody. The position predicted for full-length Sor4-GFP is indicated. *Δvps8a* cells accumulate more Sor4p-GFP than do wild-type cells.

(E) Confocal live microscopy of wild-type and *Δvps8a* expressing Sor4p-GFP and pulse-labeled with 5 μM FM4-64 for 5 min. A small fraction of Sor4p-GFP vesicles in wild-type cells is labeled with FM4-64, and this overlap increases in *Δvps8a*. Scale bars, 10 μm.

(F) Overlap of Sor4p-GFP with FM4-64 (M1) was calculated as in Figure 2B, using 40 non-overlapping images/sample. Error bars represent SDs.

See also Figure S3.

organelles [56–58]. In fungi and animals, the Vps8 subunit makes direct contact with Rab GTPase in a target membrane [54]. Thus, the six *VPS8* paralogs in *Tetrahymena* may confer different target specificities for distinct CORVET complexes. Moreover, three of the four core subunits found in both CORVET and HOPS, though not the CORVET-specific subunit

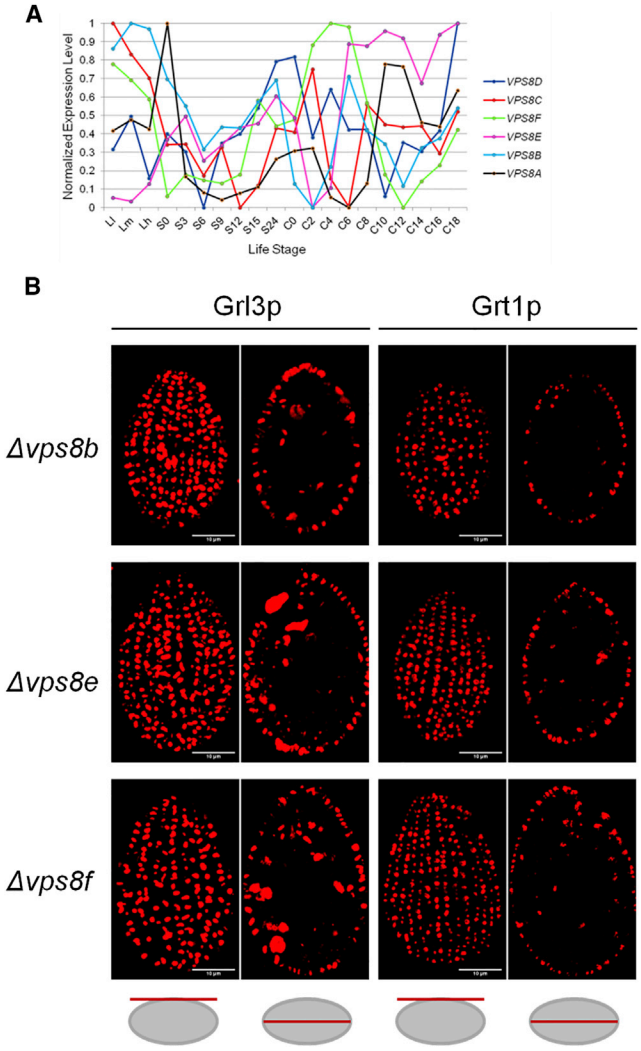

Figure 5. Expansion in Ciliates of CORVET *VPS8* Genes

(A) Expression profiles of the six *T. thermophila VPS8* paralogs, displayed as in Figure 1C, shows that each paralog has distinct expression peaks, and only *VPS8A* (black line) shows the profile associated with mucocyst formation (Figure 1C). Expression data were downloaded from the Tetrahymena Functional Genomics Database (TFGD; http://tfgd.ihb.ac.cn/).

(B) Non-essential paralogs *VPSB*, *E*, and *F* are dispensable for mucocyst formation. *Δvps8b*, *Δvps8e*, and *Δvps8f* cells were immunolabeled with antibodies against Grl3p or Grt1p, followed by Texas red-conjugated goat anti-mouse. All strains maintained wild-type patterns of docked mucocysts. Surface and cross sections are indicated at the panel bottom. Scale bars, 10 μm. See also Figure S4.

VPS3, are also present as multiple paralogs in *T. thermophila*: *VPS16*, *18*, and *33* [49]. To ask whether Vps8ap-containing complexes are enriched in specific paralogs of other subunits, we performed pull-downs from cells transformed to express Vps8a-ZZ-FLAG in combination with a hemagglutinin (HA)-tagged copy of either Vps16a or b. Our results indicated that Vps8ap preferentially associated with Vps16bp (Figures S5A and S5B), suggesting that different CORVET complexes contain subunits with distinct paralogs. Hence, different CORVET paralogs may, in a combinatorial fashion, partition endosomal traffic among a variety of pathways.

Vps8a Is Associated with Rab7-Positive Endosomes

If the Sor4p-Grt1p-positive vesicles in *Δvps8a* cells are related to early endosomes, we would expect them to label readily with an endosomal tracer. However, they showed only limited overlap with FM4-64 (Figures 4E and 4F). We considered this result in light of the fact that *T. thermophila* lacks all subunits specific for the HOPS complex. By analyzing genomes and transcriptomes from across the diversity of ciliates, we found that loss of HOPS occurred after divergence of Spirotrichea from the subsequent lineages, including Oligohymenophorea, the group in which the expansion of CORVET paralogs took place (Figure 6A). This raised the possibility that novel CORVET complexes were providing HOPS-like functions and acting at late endosomes. To test this idea, we looked at co-localization with RabGTPases.

In animal cells, CORVET is associated with Rab5-positive early endosomes, which mature to Rab7- and HOPS-associated late endosomes [20]. CORVET also associates with Rab5 in the fungi *S. cerevisiae* and *Aspergillus nidulans*, which in the latter marks early endosomes [21, 60]. Rab22 is the Rab paralog most closely related to Rab5 [61]. *T. thermophila* lacks a clear Rab5 ortholog, but Rab22A co-localizes extensively with the bulk endosomal tracer FM4-64, consistent with it marking early endosomes, while the sole Rab7 homolog associates significantly with vesicles that accumulate LysoTracker and likely represent late endosomes/lysosomes [62].

We therefore analyzed co-localization of mNeon-tagged Vps8a with mCherry-tagged Rab22A or Rab7. Vps8a-mNeon was integrated to fully replace *VPS8A* at the endogenous locus. The tagged protein was functional, judging by the fact that the cells accumulated docked mucocysts, and mucocyst secretion was nearly equivalent to wild-type (Figures S5C–S5E). Strikingly, Vps8a showed roughly 50% co-localization with Rab7 but only ~10% co-localization with Rab22A (Figures 6B and 6C). Similarly, Sor4 showed roughly 50% co-localization with Rab7 and, importantly, 64% co-localization with Vps8a (Figures S5F–S5I). Moreover, Sor4 and Rab7 co-localized in clustered vesicles in the *Δvps8a* background (Figures S5F and S5G). These data, combined with our results on FM4-64 accumulation, strongly suggest that the Vps8a-containing CORVET complex in *T. thermophila* acts primarily at a Sor4-positive late endosomal compartment.

We then asked whether the absence of Vps8ap led to a change in the Rab22A or Rab7 compartments compared to wild-type. To this end, we characterized the size and number of Rab22A and Rab7 puncta in both live and fixed wild-type and *Δvps8a* cells, and we measured particle number and size distributions in z stacks of the fixed samples. The Rab22A-positive puncta had a similar distribution and appearance in the mutant and wild-type (Figures 6D and S6A). Vesicles in the medium and larger size classes were more numerous in the mutant (Figure S6B). Rab7-positive structures showed a more striking difference in the wild-type versus *Δvps8a*. In wild-type, Rab7 puncta were dispersed in the cytoplasm, but in *Δvps8a* they formed large clusters (Figures 6E and S6C). Consistent with this, we measured a mild increase in the number of Rab7 small, medium, and large puncta in *Δvps8a*, but a significantly larger increase in a size class that corresponded to clusters (Figure S6D). This was also seen in live cells (data not shown).

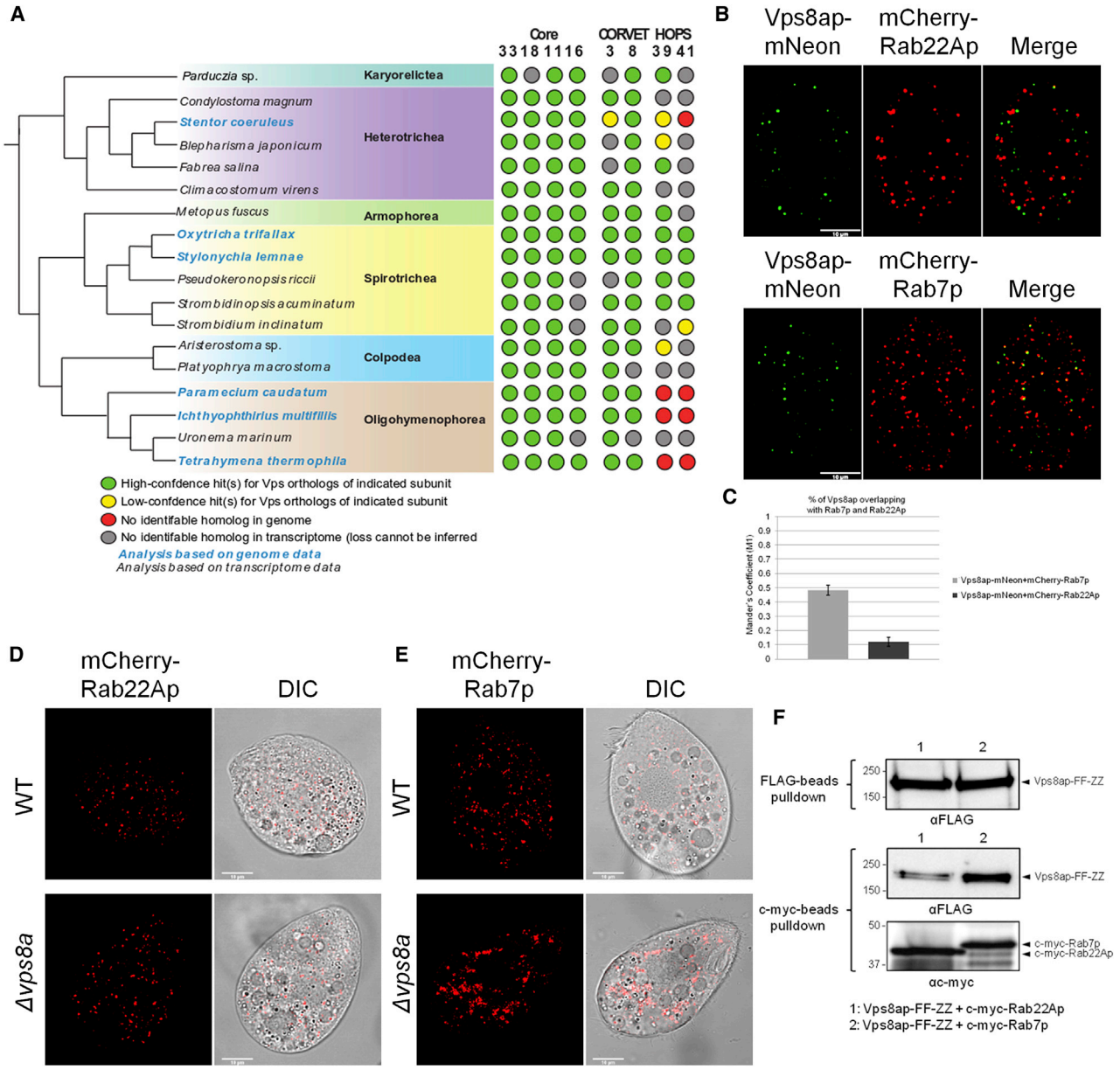

Figure 6. Association of Vps8ap with Rab7 Endosomes

(A) Distribution of HOPS/CORVET subunits across ciliate diversity. Relationships between ciliate species, based on [59], are depicted by the evolutionary tree on the left (not to scale), with phylogenetic class indicated in bold. The dotplot on the right depicts the presence/absence of the indicated subunit within each species, as defined in the STAR Methods. Gene IDs are listed in Table S1.

(B) Cells were transformed to co-express mNeon-tagged Vps8ap at the endogenous locus together with either the Rab5 homolog mCherry-Rab22Ap (upper panel) or mCherry-Rab7p (lower panel), respectively. Rab transgene overexpression was induced with 1 μg/mL $CdCl_2$ for 2.5 hr in SPP. Scale bars, 10 μm.

(C) The overlap between Vps8ap-mNeon and each Rab-GTPase (M1) was measured as in Figure 2B. Vps8a-mNeon overlapped ~50% with mCherry-Rab7 but only ~12% with mCherry-Rab22A. The mean M1 values and SDs (error bars) were derived from 65 and 66 non-overlapping images for Rab22Ap and Rab7p samples, respectively.

(D and E) Endosome distribution in wild-type versus *Δvps8a* cells. Shown are single frames from time-lapse movies of wild-type and *Δvps8a* cells, overexpressing mCherry-Rab22Ap (D) and mCherry-Rab7p (E). Cells were transferred to S-medium and mCherry-Rab transgene overexpression was induced as in (B). Rab22Ap-positive endosomes have a similar distribution in wild-type and *Δvps8a*, but Rab7p-positive endosomes form large clusters in *Δvps8a* cells. Scale bars, 10 μm.

(F) Co-immunoisolation of Vps8ap and c-*myc*-Rabs. Cells were transformed to express Vps8ap-FF-ZZ (FLAG-ZZ domain) together with either c-*myc*-Rab22Ap or c-*myc*-Rab7p, via gene replacement at the endogenous loci. Detergent lysates were incubated with bead-bound anti-c-*myc* or anti-FLAG Abs, and bead eluates were analyzed by SDS-PAGE and western blotting using anti-myc or anti-FLAG antibodies. The top panel shows total Vps8a-FF-ZZ in each cell line, while the bottom panel shows total myc-Rab22a or myc-Rab7 in each cell line. The middle panel shows Vps8a-FF-ZZ that was immuno-isolated via an interaction with Rab22A (left lane) or Rab7 (right lane). Vps8ap preferentially interacts with Rab7p.

See also Figures S5 and S6.

Finally, we looked for evidence that Vps8a is physically associated with Rab7. We transformed cells to express Vps8a-FF-ZZ and either myc-Rab22A or myc-Rab7, with all tagged proteins expressed from their endogenous loci. In pull-downs of Rab7, but not Rab22A, we saw robust co-isolation of Vps8a (Figure 6F). This result strongly supports the idea that Vps8a interacts preferentially with Rab7, either directly or via another subunit of a specific CORVET complex.

DISCUSSION

Guided by results of a forward genetic screen, we discovered that mucocyst formation in *T. thermophila* requires the *VPS8A* gene, a subunit of the CORVET complex. The *Δvps8a* cells accumulate vesicles that contain the mucocyst sorting receptor Sor4p as well as several cargo proteins, including Grt1p, which in wild-type cells are delivered to immature mucocysts. These vesicles are likely to represent transient intermediates in mucocyst biogenesis that accumulate in the mutant because tethering and fusion to their target is inhibited. Thus, we hypothesize that the primary defect in *Δvps8a* is in the fate of endosome-related vesicles that deliver proteins, including maturation factors, to immature mucocysts. The involvement of CORVET in mucocyst formation reinforces and extends the prior evidence that this pathway relies on endosomal trafficking [47, 48]. Our results support a model of parallel sorting/delivery of mucocyst contents: GRL proteins are segregated and sorted from other secretory cargo based on aggregation, while GRT/IGR proteins, as well as the processing cathepsin Cth3p, are delivered via endosomes as ligands of the Sor4p receptor.

An additional defect was previously documented in the SB281 strain, which we discovered also bears a mutation in *VPS8A*. Starved SB281 cells show constitutive secretion of pro-GRL proteins that, in wild-type cells, are instead efficiently stored and then proteolytically processed [52]. Interestingly, perturbing the maturation of regulated secretory compartments in animal cells also leads to aberrant constitutive secretion [63]. In *Tetrahymena*, a fraction of the mucocyst cargo proteins in the mutant cells is also found in degradative compartments, which could reflect autophagy of abortive mucocyst intermediates.

CORVET as well as HOPS genes are found throughout eukaryotes [25], implying that both complexes arose during pre-LECA evolution, with duplication and co-evolution of genes producing two complexes whose subtly altered specificities contributed to differentiation of endosomal trafficking pathways. Prior to this paper, functional characterization of CORVET has only been reported in a single eukaryotic lineage, the Opisthokonts (including animals and fungi), where it associates with Rab5/VPS21-positive endosomes. HOPS has recently been characterized in a second lineage, plants (lineage Archaeplastida), where it appears to function at late endosomes/vacuoles [64, 65]. We previously noted the unusual absence of HOPS-specific subunits in genomes of two ciliates, *T. thermophila* and *Ichthyophthirius multifiliis* [49]. By analyzing additional ciliate genomes and transcriptomes, we can now infer that those losses likely occurred prior to the diversification of the Oligohymenophorea. Though loss of genes cannot be strictly concluded from transcriptomic data, the presence of HOPS components in both genomes and transcriptomes from outside the Oligohymenophorea implies that gene losses occurred as a group-specific adaptation. These losses are unlikely to reflect an evolutionary reduction in the complexity of endosomal pathways: *T. thermophila* expresses at least three Rab8 paralogs and six likely Rab11 paralogs, and HOPS-specific losses are paralleled by proliferation of both core and CORVET-specific subunits. The six *VPS8* paralogs may be specialized for distinct endocytic pathways, reflected by unique peaks within each expression profile. We found that only the *VPS8A* paralog is essential for mucocyst formation, while no other non-essential paralogs showed mucocyst phenotypes. Moreover, two of the *VPS8* paralogs are essential, while the others have no growth phenotypes but result in altered endocytic compartments.

The function of HOPS/CORVET depends on each complex bridging two different vesicles by making multivalent contacts with vesicle constituents, including Rabs, SNAREs, coat proteins, and phospholipids [66, 67]. In the prevailing model for yeast CORVET, the recognition of Rabs on the two target membranes occurs via the Vps8 and Vps3 subunits [68–73]. Thus, in ciliates, the expansion of VPS8 paralogs may have contributed to specifying a large set of endolysosomal compartments, if different VPS8 paralogs preferentially bind to different Rabs. Consistent with this idea, RabGTPases also underwent expansions of paralogs in some Oligohymenophorea [62, 74–76]. Intriguingly, the second well-established Rab-binding subunit in the yeast model, Vps3, is encoded by a single gene in *T. thermophila*, suggesting that additional specificity may be determined by interactions with other vesicle proteins, e.g., SNAREs that also expanded in Oligohymenophorea. In yeast, both Vps16 and Vps33 are involved in binding to SNAREs [77], and both genes are encoded by multiple paralogs in *T. thermophila*. While we have not yet physically characterized a *T. thermophila* CORVET complex, we found that Vps8a could be robustly co-precipitated with the core subunit Vps16b, consistent with the idea that the subunits assemble as they do in other studied organisms. It is worth noting, however, that functional CORVET sub-complexes have been reported in *Drosophila* [78]. How many distinct CORVET complexes exist in *Tetrahymena*? In addition to six *VSP8* paralogs, *Tetrahymena* also expresses two paralogs each of the core subunits *VPS16* and *33* and four paralogs of core subunit *VPS18*, so, in theory, it could generate 96 compositionally distinct CORVET complexes.

A key finding was that Vps8a preferentially co-localizes and can be co-precipitated with the late endosomal Rab7 rather than with the early endosomal Rab22. The basis for the change in *VPS8* specificity, e.g., whether Vps8a directly interacts with Rab7 or whether this is via another CORVET subunit, remains to be determined. Given that loss of HOPS occurred after the split between Oligohymenophorea and Spirotrichea/Armophorea/Litostomatea (SAL) but before the diversification of Oligohymenophorea, an attractive hypothesis is that new CORVET paralogs in this lineage took on HOPS-like specificity. Since the family of Rab GTPases also underwent marked expansion in ciliates, the change in CORVET specificity may reveal a broader remodeling of endosomal determinants.

The precise role of Vps8a in *Tetrahymena* is not yet clear. The *Δvps8a* cells show marked clustering of Rab7-positive vesicles. Interestingly, these are unlikely to be strongly acidic since they do not label with LysoTracker, i.e., there is no

comparable clustering of LysoTracker-positive vesicles in the mutant cells. Surprisingly, Vps8a did not appreciably co-localize with Grl3p in immature or mature mucocysts. The absence of Vps8a at the presumed acceptor compartment may indicate that the tethering step per se is very short lived. However, another possibility is that the Sor4p-GFP vesicles bearing mucocyst cargo first undergo Vps8a-dependent fusion with an unknown compartment, prior to cargo delivery at immature mucocysts.

In animals, mechanisms involved in lysosome biogenesis are deployed to generate a remarkably diverse collection of complex secretory organelles, including melanosomes, pigment granules, Weibel-Palade bodies, and T cell lytic granules [8]. In the apicomplexan *Toxoplasma gondii*, formation of three types of secretory organelles, including rhoptries, was inhibited by knockdown of VPS11, a core subunit of both HOPS and CORVET [40]. Although the authors assumed that CORVET is absent in *T. gondii*, our previous analysis of HOPS and CORVET subunit evolution in apicomplexans would argue that phenotypes in *Toxoplasma* VPS11 knockdown cells could reflect the loss or modified function of either or both complexes [25]. Most importantly, the requirement for CORVET and/or HOPS underscores the relevance of LRO mechanisms in apicomplexan-regulated secretion. Moreover, regulated secretion in dinoflagellates is also likely to share a common origin with ciliates [79].

Tetrahymena mucocysts represent an elaborate secretory compartment, generated via a complex stepwise program. GRL proteins assemble in the mucocyst lumen to form an elongated crystal, which expands in a spring-like fashion during exocytosis when exposed to extracellular calcium [80]. Importantly, assembly occurs only after the pro-GRL proteins undergo processing, and the key processing enzyme Cth3p is delivered to mucocysts via the *SOR4/STX7L1/VPS8A*-dependent pathway [47, 48, 81]. In these cells, mechanisms of LRO biogenesis are thus used to process secretory cargo using lysosome-related hydrolases to assemble calcium-sensitive springs. Our results, taken together with findings in apicomplexans, indicate that not only animals but also protists in the distantly related and globally important Alveolate lineage adapted LRO-based strategies to enhance their secretory responses.

STAR★METHODS

Detailed methods are provided in the online version of this paper and include the following:

- KEY RESOURCES TABLE
- CONTACT FOR REAGENT AND RESOURCE SHARING
- EXPERIMENTAL MODEL AND SUBJECT DETAILS
  - Cell strains and culture conditions
- METHOD DETAILS
  - Genetic methods
  - Testing assortants for exocytosis competence
  - Genomic DNA extraction
  - Whole genome sequencing
  - Sequence alignment
  - Variant discovery
  - Candidate screening
  - Transcription profiles
  - Generation of VPS8 knockout strains
  - RT-PCR assessment of VPS8 disruption, and intron retention in the VPS8A transcript of UC616
  - Expression of Vps8ap-GFP in mutant strains
  - Expression of Grl3p-GFP, Cth3p-GFP and Sor4p-GFP at the corresponding endogenous locus in *Δvps8a*
  - Endogenous tagging of VPS8A with mNeon
  - Endogenous tagging of VPS8A with FF-ZZ tag
  - Expression of Vps16ap-HA and Vps16bp-HA
  - Co-expression of Sor4p-mCherry, c-*myc*-Rab22Ap and c-*myc*-Rab7p with tagged Vps8ap
  - Expression of mCherry-Rab7p, mCherry-Rab22Ap, Igr1p-GFP and Stx7l1p-GFP
  - Biolistic transformation
  - Fluorescence and Immunofluorescence microscopy
  - Live cell imaging
  - Labeling endocytic and acidic compartments with FM4-64 and LysoTracker
  - Electron microscopy
  - CLEM imaging
  - Dibucaine assay
  - Immunoprecipitation
  - Co-immunoprecipitation
  - Western blotting
  - Homology searching and Phylogenetic tree construction
- QUANTIFICATION AND STATISTICAL ANALYSIS
  - Colocalization analysis
  - Particle analysis

SUPPLEMENTAL INFORMATION

Supplemental Information includes six figures and four tables and can be found with this article online at https://doi.org/10.1016/j.cub.2018.01.047.

ACKNOWLEDGMENTS

D.S. and A.P.T. would like to thank Harsimran Kaur for the mCherry-RAB22A and mCherry-RAB7 constructs; Lev Tsypin and Harsimran Kaur for valuable discussion; Vytas Bindokas and Christine Labno, as well as Yimei Chen, for assistance with light and electron microscopy, respectively, at University of Chicago Core Facilities; K. Mochizuki (Institute of Human Genetics, CNRS-University of Montpellier, France) for NEO4 plasmids; and J. Frankel (University of Iowa, Iowa City) for hybridomas 5E9 and 4D11. E.R. and J.B.D. thank Michael Lynch (Arizona State University) for access to *P. caudatum* genomes. Work in T.H.'s laboratory was supported by JSPS Kakenhi grants JP24570227 and JP15K07066 to M.I. and JP26291007, JP25116006, and JP15K21730 to T.H. E.R. was supported by an Alberta Innovates - Technology Futures Graduate Student Scholarship and a Vanier Canada Graduate Scholarship. Work in D.H.L.'s laboratory was supported by National Sciences and Engineering Research Council of Canada grant 6544-201. Work in J.K.P.'s laboratory was supported by the Howard Hughes Medical Foundation and NIH 1RO1ES025009. Work in J.B.D.'s laboratory was supported by a Discovery Grant from the Natural Sciences and Engineering Research Council of Canada (RES0021028), and J.B.D. is the Canada Research Chair (Tier II) in Evolutionary Cell Biology. Work in A.P.T.'s laboratory was supported by NIH 1RO1GM105783.

AUTHOR CONTRIBUTIONS

Conceptualization, D.S., A.P.T., E.R., and J.B.D.; Methodology, D.S., G.R.B., A.P.T., M.I., T.H., E.R., J.B.D., X.L., and J.K.P.; Formal Analysis, D.S., E.R., and

X.L.; Investigation, D.S., E.R., H.O., M.I., G.R.B., and C.K.; Resources, W.A.B., D.H.L., J.K.P., T.H., J.B.D., and A.P.T.; Writing – Original Draft, D.S., E.R., X.L., M.I., T.H., J.B.D., and A.P.T.; Writing – Review & Editing, D.H.L.; Visualization, D.S., E.R., H.O., and M.I.; Supervision, A.P.T., J.B.D., and T.H.; Funding Acquisition, A.P.T., T.H., J.B.D., D.H.L., and J.K.P.

DECLARATION OF INTERESTS

The authors declare no competing interests.

Received: September 14, 2017
Revised: December 9, 2017
Accepted: January 17, 2018
Published: February 22, 2018

REFERENCES

1. Palade, G. (1975). Intracellular aspects of the process of protein synthesis. Science *189*, 347–358.
2. Keller, P., and Simons, K. (1997). Post-Golgi biosynthetic trafficking. J. Cell Sci. *110*, 3001–3009.
3. Burgoyne, R.D., and Morgan, A. (1993). Regulated exocytosis. Biochem. J. *293*, 305–316.
4. Tran, D.T., and Ten Hagen, K.G. (2017). Real-time insights into regulated exocytosis. J. Cell Sci. *130*, 1355–1363.
5. Orci, L., Ravazzola, M., Amherdt, M., Perrelet, A., Powell, S.K., Quinn, D.L., and Moore, H.P. (1987). The trans-most cisternae of the Golgi complex: a compartment for sorting of secretory and plasma membrane proteins. Cell *51*, 1039–1051.
6. Arvan, P., and Castle, D. (1998). Sorting and storage during secretory granule biogenesis: looking backward and looking forward. Biochem. J. *332*, 593–610.
7. Luzio, J.P., Hackmann, Y., Dieckmann, N.M., and Griffiths, G.M. (2014). The biogenesis of lysosomes and lysosome-related organelles. Cold Spring Harb. Perspect. Biol. *6*, a016840.
8. Marks, M.S., Heijnen, H.F., and Raposo, G. (2013). Lysosome-related organelles: unusual compartments become mainstream. Curr. Opin. Cell Biol. *25*, 495–505.
9. Bonifacino, J.S. (2004). Insights into the biogenesis of lysosome-related organelles from the study of the Hermansky-Pudlak syndrome. Ann. N Y Acad. Sci. *1038*, 103–114.
10. Raposo, G., Marks, M.S., and Cutler, D.F. (2007). Lysosome-related organelles: driving post-Golgi compartments into specialisation. Curr. Opin. Cell Biol. *19*, 394–401.
11. Starcevic, M., Nazarian, R., and Dell'Angelica, E.C. (2002). The molecular machinery for the biogenesis of lysosome-related organelles: lessons from Hermansky-Pudlak syndrome. Semin. Cell Dev. Biol. *13*, 271–278.
12. Gautam, R., Novak, E.K., Tan, J., Wakamatsu, K., Ito, S., and Swank, R.T. (2006). Interaction of Hermansky-Pudlak Syndrome genes in the regulation of lysosome-related organelles. Traffic *7*, 779–792.
13. Wasmeier, C., Romao, M., Plowright, L., Bennett, D.C., Raposo, G., and Seabra, M.C. (2006). Rab38 and Rab32 control post-Golgi trafficking of melanogenic enzymes. J. Cell Biol. *175*, 271–281.
14. Hermey, G. (2009). The Vps10p-domain receptor family. Cell. Mol. Life Sci. *66*, 2677–2689.
15. Marcusson, E.G., Horazdovsky, B.F., Cereghino, J.L., Gharakhanian, E., and Emr, S.D. (1994). The sorting receptor for yeast vacuolar carboxypeptidase Y is encoded by the VPS10 gene. Cell *77*, 579–586.
16. Orr, A., Song, H., Rusin, S.F., Kettenbach, A.N., and Wickner, W. (2017). HOPS catalyzes the interdependent assembly of each vacuolar SNARE into a SNARE complex. Mol. Biol. Cell *28*, 975–983.
17. Pulipparacharuvil, S., Akbar, M.A., Ray, S., Sevrioukov, E.A., Haberman, A.S., Rohrer, J., and Krämer, H. (2005). Drosophila Vps16A is required for trafficking to lysosomes and biogenesis of pigment granules. J. Cell Sci. *118*, 3663–3673.
18. Balderhaar, H.J., and Ungermann, C. (2013). CORVET and HOPS tethering complexes - coordinators of endosome and lysosome fusion. J. Cell Sci. *126*, 1307–1316.
19. Solinger, J.A., and Spang, A. (2013). Tethering complexes in the endocytic pathway: CORVET and HOPS. FEBS J. *280*, 2743–2757.
20. Perini, E.D., Schaefer, R., Stöter, M., Kalaidzidis, Y., and Zerial, M. (2014). Mammalian CORVET is required for fusion and conversion of distinct early endosome subpopulations. Traffic *15*, 1366–1389.
21. Horazdovsky, B.F., Cowles, C.R., Mustol, P., Holmes, M., and Emr, S.D. (1996). A novel RING finger protein, Vps8p, functionally interacts with the small GTPase, Vps21p, to facilitate soluble vacuolar protein localization. J. Biol. Chem. *271*, 33607–33615.
22. Richardson, S.C., Winistorfer, S.C., Poupon, V., Luzio, J.P., and Piper, R.C. (2004). Mammalian late vacuole protein sorting orthologues participate in early endosomal fusion and interact with the cytoskeleton. Mol. Biol. Cell *15*, 1197–1210.
23. Rink, J., Ghigo, E., Kalaidzidis, Y., and Zerial, M. (2005). Rab conversion as a mechanism of progression from early to late endosomes. Cell *122*, 735–749.
24. Klöpper, T.H., Kienle, N., Fasshauer, D., and Munro, S. (2012). Untangling the evolution of Rab G proteins: implications of a comprehensive genomic analysis. BMC Biol. *10*, 71.
25. Klinger, C.M., Klute, M.J., and Dacks, J.B. (2013). Comparative genomic analysis of multi-subunit tethering complexes demonstrates an ancient pan-eukaryotic complement and sculpting in Apicomplexa. PLoS ONE *8*, e76278.
26. Field, M.C., Gabernet-Castello, C., and Dacks, J.B. (2007). Reconstructing the evolution of the endocytic system: insights from genomics and molecular cell biology. Adv. Exp. Med. Biol. *607*, 84–96.
27. Diekmann, Y., Seixas, E., Gouw, M., Tavares-Cadete, F., Seabra, M.C., and Pereira-Leal, J.B. (2011). Thousands of rab GTPases for the cell biologist. PLoS Comput. Biol. *7*, e1002217.
28. Koumandou, V.L., Wickstead, B., Ginger, M.L., van der Giezen, M., Dacks, J.B., and Field, M.C. (2013). Molecular paleontology and complexity in the last eukaryotic common ancestor. Crit. Rev. Biochem. Mol. Biol. *48*, 373–396.
29. Rosati, G., and Modeo, L. (2003). Extrusomes in ciliates: diversification, distribution, and phylogenetic implications. J. Eukaryot. Microbiol. *50*, 383–402.
30. Gavelis, G.S., Wakeman, K.C., Tillmann, U., Ripken, C., Mitarai, S., Herranz, M., Özbek, S., Holstein, T., Keeling, P.J., and Leander, B.S. (2017). Microbial arms race: Ballistic "nematocysts" in dinoflagellates represent a new extreme in organelle complexity. Sci. Adv. *3*, e1602552.
31. Sharma, P., and Chitnis, C.E. (2013). Key molecular events during host cell invasion by Apicomplexan pathogens. Curr. Opin. Microbiol. *16*, 432–437.
32. Wessenberg, H., and Antipa, G. (1970). Capture and ingestion of Paramecium by Didinium nasutum. J. Protozool. *17*, 250–270.
33. Harumoto, T., and Miyake, A. (1991). Defensive function of trichocysts in Paramecium. J. Exp. Zool. *260*, 84–92.
34. Knoll, G., Haacke-Bell, B., and Plattner, H. (1991). Local trichocyst exocytosis provides an efficient escape mechanism for Paramecium cells. Eur. J. Protistol. *27*, 381–385.
35. Buonanno, F., Anesi, A., Guella, G., Kumar, S., Bharti, D., La Terza, A., Quassinti, L., Bramucci, M., and Ortenzi, C. (2014). Chemical offense by means of toxicysts in the freshwater ciliate, Coleps hirtus. J. Eukaryot. Microbiol. *61*, 293–304.
36. Jimenez-Ruiz, E., Morlon-Guyot, J., Daher, W., and Meissner, M. (2016). Vacuolar protein sorting mechanisms in apicomplexan parasites. Mol. Biochem. Parasitol. *209*, 18–25.

37. Ngô, H.M., Yang, M., and Joiner, K.A. (2004). Are rhoptries in Apicomplexan parasites secretory granules or secretory lysosomal granules? Mol. Microbiol. *52*, 1531–1541.

38. Sloves, P.J., Delhaye, S., Mouveaux, T., Werkmeister, E., Slomianny, C., Hovasse, A., Dilezitoko Alayi, T., Callebaut, I., Gaji, R.Y., Schaeffer-Reiss, C., et al. (2012). Toxoplasma sortilin-like receptor regulates protein transport and is essential for apical secretory organelle biogenesis and host infection. Cell Host Microbe *11*, 515–527.

39. Kremer, K., Kamin, D., Rittweger, E., Wilkes, J., Flammer, H., Mahler, S., Heng, J., Tonkin, C.J., Langsley, G., Hell, S.W., et al. (2013). An overexpression screen of Toxoplasma gondii Rab-GTPases reveals distinct transport routes to the micronemes. PLoS Pathog. *9*, e1003213.

40. Morlon-Guyot, J., Pastore, S., Berry, L., Lebrun, M., and Daher, W. (2015). Toxoplasma gondii Vps11, a subunit of HOPS and CORVET tethering complexes, is essential for the biogenesis of secretory organelles. Cell. Microbiol. *17*, 1157–1178.

41. Sakura, T., Sindikubwabo, F., Oesterlin, L.K., Bousquet, H., Slomianny, C., Hakimi, M.A., Langsley, G., and Tomavo, S. (2016). A Critical Role for Toxoplasma gondii Vacuolar Protein Sorting VPS9 in Secretory Organelle Biogenesis and Host Infection. Sci. Rep. *6*, 38842.

42. Warren, A., Patterson, D.J., Dunthorn, M., Clamp, J.C., Achilles-Day, U.E.M., Aescht, E., Al-Farraj, S.A., Al-Quraishy, S., Al-Rasheid, K., Carr, M., et al. (2017). Beyond the "Code": A Guide to the Description and Documentation of Biodiversity in Ciliated Protists (Alveolata, Ciliophora). J. Eukaryot. Microbiol. *64*, 539–554.

43. Guerrier, S., Plattner, H., Richardson, E., Dacks, J.B., and Turkewitz, A.P. (2017). An evolutionary balance: conservation vs innovation in ciliate membrane trafficking. Traffic *18*, 18–28.

44. Turkewitz, A.P. (2004). Out with a bang! Tetrahymena as a model system to study secretory granule biogenesis. Traffic *5*, 63–68.

45. Bowman, G.R., Smith, D.G., Michael Siu, K.W., Pearlman, R.E., and Turkewitz, A.P. (2005). Genomic and proteomic evidence for a second family of dense core granule cargo proteins in Tetrahymena thermophila. J. Eukaryot. Microbiol. *52*, 291–297.

46. Bowman, G.R., Elde, N.C., Morgan, G., Winey, M., and Turkewitz, A.P. (2005). Core formation and the acquisition of fusion competence are linked during secretory granule maturation in Tetrahymena. Traffic *6*, 303–323.

47. Briguglio, J.S., Kumar, S., and Turkewitz, A.P. (2013). Lysosomal sorting receptors are essential for secretory granule biogenesis in Tetrahymena. J. Cell Biol. *203*, 537–550.

48. Kaur, H., Sparvoli, D., Osakada, H., Iwamoto, M., Haraguchi, T., and Turkewitz, A.P. (2017). An endosomal syntaxin and the AP-3 complex are required for formation and maturation of candidate lysosome-related secretory organelles (mucocysts) in Tetrahymena thermophila. Mol. Biol. Cell *28*, 1551–1564.

49. Woo, Y.H., Ansari, H., Otto, T.D., Klinger, C.M., Kolisko, M., Michálek, J., Saxena, A., Shanmugam, D., Tayyrov, A., Veluchamy, A., et al. (2015). Chromerid genomes reveal the evolutionary path from photosynthetic algae to obligate intracellular parasites. eLife *4*, e06974.

50. Kontur, C., Kumar, S., Lan, X., Pritchard, J.K., and Turkewitz, A.P. (2016). Whole genome sequencing identifies a novel factor required for secretory granule maturation in Tetrahymena thermophila. G3 (Bethesda) *6*, 2505–2516.

51. Orias, E., Flacks, M., and Satir, B.H. (1983). Isolation and ultrastructural characterization of secretory mutants of Tetrahymena thermophila. J. Cell Sci. *64*, 49–67.

52. Bowman, G.R., and Turkewitz, A.P. (2001). Analysis of a mutant exhibiting conditional sorting to dense core secretory granules in Tetrahymena thermophila. Genetics *159*, 1605–1616.

53. Xiong, J., Lu, Y., Feng, J., Yuan, D., Tian, M., Chang, Y., Fu, C., Wang, G., Zeng, H., and Miao, W. (2013). Tetrahymena functional genomics database (TetraFGD): an integrated resource for Tetrahymena functional genomics. Database (Oxford) *2013*, bat008.

54. Markgraf, D.F., Ahnert, F., Arlt, H., Mari, M., Peplowska, K., Epp, N., Griffith, J., Reggiori, F., and Ungermann, C. (2009). The CORVET subunit Vps8 cooperates with the Rab5 homolog Vps21 to induce clustering of late endosomal compartments. Mol. Biol. Cell *20*, 5276–5289.

55. Viotti, C., Bubeck, J., Stierhof, Y.D., Krebs, M., Langhans, M., van den Berg, W., van Dongen, W., Richter, S., Geldner, N., Takano, J., et al. (2010). Endocytic and secretory traffic in Arabidopsis merge in the trans-Golgi network/early endosome, an independent and highly dynamic organelle. Plant Cell *22*, 1344–1357.

56. Balderhaar, H.J., Lachmann, J., Yavavli, E., Bröcker, C., Lürick, A., and Ungermann, C. (2013). The CORVET complex promotes tethering and fusion of Rab5/Vps21-positive membranes. Proc. Natl. Acad. Sci. USA *110*, 3823–3828.

57. Kümmel, D., and Ungermann, C. (2014). Principles of membrane tethering and fusion in endosome and lysosome biogenesis. Curr. Opin. Cell Biol. *29*, 61–66.

58. Peplowska, K., Markgraf, D.F., Ostrowicz, C.W., Bange, G., and Ungermann, C. (2007). The CORVET tethering complex interacts with the yeast Rab5 homolog Vps21 and is involved in endo-lysosomal biogenesis. Dev. Cell *12*, 739–750.

59. Gentekaki, E., Kolisko, M., Boscaro, V., Bright, K.J., Dini, F., Di Giuseppe, G., Gong, Y., Miceli, C., Modeo, L., Molestina, R.E., et al. (2014). Large-scale phylogenomic analysis reveals the phylogenetic position of the problematic taxon Protocruzia and unravels the deep phylogenetic affinities of the ciliate lineages. Mol. Phylogenet. Evol. *78*, 36–42.

60. Abenza, J.F., Galindo, A., Pantazopoulou, A., Gil, C., de los Ríos, V., and Peñalva, M.A. (2010). Aspergillus RabB Rab5 integrates acquisition of degradative identity with the long distance movement of early endosomes. Mol. Biol. Cell *21*, 2756–2769.

61. Elias, M., Brighouse, A., Gabernet-Castello, C., Field, M.C., and Dacks, J.B. (2012). Sculpting the endomembrane system in deep time: high resolution phylogenetics of Rab GTPases. J. Cell Sci. *125*, 2500–2508.

62. Bright, L.J., Kambesis, N., Nelson, S.B., Jeong, B., and Turkewitz, A.P. (2010). Comprehensive analysis reveals dynamic and evolutionary plasticity of Rab GTPases and membrane traffic in Tetrahymena thermophila. PLoS Genet. *6*, e1001155.

63. Sirkis, D.W., Edwards, R.H., and Asensio, C.S. (2013). Widespread dysregulation of peptide hormone release in mice lacking adaptor protein AP-3. PLoS Genet. *9*, e1003812.

64. Vukašinović, N., and Žárský, V. (2016). Tethering complexes in the Arabidopsis endomembrane system. Front. Cell Dev. Biol. *4*, 46.

65. Tan, X., Wei, J., Li, B., Wang, M., and Bao, Y. (2017). AtVps11 is essential for vacuole biogenesis in embryo and participates in pollen tube growth in Arabidopsis. Biochem. Biophys. Res. Commun. *491*, 794–799.

66. Chou, H.T., Dukovski, D., Chambers, M.G., Reinisch, K.M., and Walz, T. (2016). CATCHR, HOPS and CORVET tethering complexes share a similar architecture. Nat. Struct. Mol. Biol. *23*, 761–763.

67. Cabrera, M., Langemeyer, L., Mari, M., Rethmeier, R., Orban, I., Perz, A., Bröcker, C., Griffith, J., Klose, D., Steinhoff, H.J., et al. (2010). Phosphorylation of a membrane curvature-sensing motif switches function of the HOPS subunit Vps41 in membrane tethering. J. Cell Biol. *191*, 845–859.

68. Dulubova, I., Yamaguchi, T., Wang, Y., Südhof, T.C., and Rizo, J. (2001). Vam3p structure reveals conserved and divergent properties of syntaxins. Nat. Struct. Biol. *8*, 258–264.

69. Sato, T.K., Rehling, P., Peterson, M.R., and Emr, S.D. (2000). Class C Vps protein complex regulates vacuolar SNARE pairing and is required for vesicle docking/fusion. Mol. Cell *6*, 661–671.

70. Stroupe, C., Collins, K.M., Fratti, R.A., and Wickner, W. (2006). Purification of active HOPS complex reveals its affinities for phosphoinositides and the SNARE Vam7p. EMBO J. *25*, 1579–1589.

71. Stroupe, C., Hickey, C.M., Mima, J., Burfeind, A.S., and Wickner, W. (2009). Minimal membrane docking requirements revealed by reconstitution of Rab GTPase-dependent membrane fusion from purified components. Proc. Natl. Acad. Sci. USA *106*, 17626–17633.

72. Ostrowicz, C.W., Bröcker, C., Ahnert, F., Nordmann, M., Lachmann, J., Peplowska, K., Perz, A., Auffarth, K., Engelbrecht-Vandré, S., and Ungermann, C. (2010). Defined subunit arrangement and rab interactions are required for functionality of the HOPS tethering complex. Traffic *11*, 1334–1346.

73. Epp, N., and Ungermann, C. (2013). The N-terminal domains of Vps3 and Vps8 are critical for localization and function of the CORVET tethering complex on endosomes. PLoS ONE *8*, e67307.

74. Saito-Nakano, Y., Nakahara, T., Nakano, K., Nozaki, T., and Numata, O. (2010). Marked amplification and diversification of products of ras genes from rat brain, Rab GTPases, in the ciliates Tetrahymena thermophila and Paramecium tetraurelia. J. Eukaryot. Microbiol. *57*, 389–399.

75. Kissmehl, R., Schilde, C., Wassmer, T., Danzer, C., Nuehse, K., Lutter, K., and Plattner, H. (2007). Molecular identification of 26 syntaxin genes and their assignment to the different trafficking pathways in paramecium. Traffic *8*, 523–542.

76. Schilde, C., Wassmer, T., Mansfeld, J., Plattner, H., and Kissmehl, R. (2006). A multigene family encoding R-SNAREs in the ciliate Paramecium tetraurelia. Traffic *7*, 440–455.

77. Lürick, A., Gao, J., Kuhlee, A., Yavavli, E., Langemeyer, L., Perz, A., Raunser, S., and Ungermann, C. (2017). Multivalent Rab interactions determine tether-mediated membrane fusion. Mol. Biol. Cell *28*, 322–332.

78. Lőrincz, P., Lakatos, Z., Varga, Á., Maruzs, T., Simon-Vecsei, Z., Darula, Z., Benkő, P., Csordás, G., Lippai, M., Andó, I., et al. (2016). MiniCORVET is a Vps8-containing early endosomal tether in Drosophila. eLife *5*, e14226.

79. Rhiel, E., Wöhlbrand, L., Rabus, R., and Voget, S. (2018). Candidates of trichocyst matrix proteins of the dinoflagellate Oxyrrhis marina. Protoplasma *255*, 217–230.

80. Verbsky, J.W., and Turkewitz, A.P. (1998). Proteolytic processing and Ca2+-binding activity of dense-core vesicle polypeptides in Tetrahymena. Mol. Biol. Cell *9*, 497–511.

81. Kumar, S., Briguglio, J.S., and Turkewitz, A.P. (2014). An aspartyl cathepsin, CTH3, is essential for proprotein processing during secretory granule maturation in Tetrahymena thermophila. Mol. Biol. Cell *25*, 2444–2460.

82. Cowan, A.T., Bowman, G.R., Edwards, K.F., Emerson, J.J., and Turkewitz, A.P. (2005). Genetic, genomic, and functional analysis of the granule lattice proteins in Tetrahymena secretory granules. Mol. Biol. Cell *16*, 4046–4060.

83. Turkewitz, A.P., Madeddu, L., and Kelly, R.B. (1991). Maturation of dense core granules in wild type and mutant *Tetrahymena thermophila*. EMBO J. *10*, 1979–1987.

84. Li, H., and Durbin, R. (2009). Fast and accurate short read alignment with Burrows-Wheeler transform. Bioinformatics *25*, 1754–1760.

85. McKenna, A., Hanna, M., Banks, E., Sivachenko, A., Cibulskis, K., Kernytsky, A., Garimella, K., Altshuler, D., Gabriel, S., Daly, M., and DePristo, M.A. (2010). The Genome Analysis Toolkit: a MapReduce framework for analyzing next-generation DNA sequencing data. Genome Res. *20*, 1297–1303.

86. Schindelin, J., Arganda-Carreras, I., Frise, E., Kaynig, V., Longair, M., Pietzsch, T., Preibisch, S., Rueden, C., Saalfeld, S., Schmid, B., et al. (2012). Fiji: an open-source platform for biological-image analysis. Nat. Methods *9*, 676–682.

87. Camacho, C., Coulouris, G., Avagyan, V., Ma, N., Papadopoulos, J., Bealer, K., and Madden, T.L. (2009). BLAST+: architecture and applications. BMC Bioinformatics *10*, 421.

88. Miller, M.A., Pfeiffer, W., and Schwartz, T. (2010). Creating the CIPRES Science Gateway for inference of large phylogenetic trees. In Gateway Computing Environments Workshop (GCE), 2010 (IEEE), pp. 1–8.

89. Stamatakis, A. (2014). RAxML version 8: a tool for phylogenetic analysis and post-analysis of large phylogenies. Bioinformatics *30*, 1312–1313.

90. Ronquist, F., and Huelsenbeck, J.P. (2003). MrBayes 3: Bayesian phylogenetic inference under mixed models. Bioinformatics *19*, 1572–1574.

91. Edgar, R.C. (2004). MUSCLE: multiple sequence alignment with high accuracy and high throughput. Nucleic Acids Res. *32*, 1792–1797.

92. Darriba, D., Taboada, G.L., Doallo, R., and Posada, D. (2011). ProtTest 3: fast selection of best-fit models of protein evolution. Bioinformatics *27*, 1164–1165.

93. Ruehle, M.D., Orias, E., and Pearson, C.G. (2016). Tetrahymena as a unicellular model eukaryote: Genetic and genomic tools. Genetics *203*, 649–665.

94. Coyne, R.S., Thiagarajan, M., Jones, K.M., Wortman, J.R., Tallon, L.J., Haas, B.J., Cassidy-Hanley, D.M., Wiley, E.A., Smith, J.J., Collins, K., et al. (2008). Refined annotation and assembly of the Tetrahymena thermophila genome sequence through EST analysis, comparative genomic hybridization, and targeted gap closure. BMC Genomics *9*, 562.

95. Eisen, J.A., Coyne, R.S., Wu, M., Wu, D., Thiagarajan, M., Wortman, J.R., Badger, J.H., Ren, Q., Amedeo, P., Jones, K.M., et al. (2006). Macronuclear genome sequence of the ciliate Tetrahymena thermophila, a model eukaryote. PLoS Biol. *4*, e286.

96. Miao, W., Xiong, J., Bowen, J., Wang, W., Liu, Y., Braguinets, O., Grigull, J., Pearlman, R.E., Orias, E., and Gorovsky, M.A. (2009). Microarray analyses of gene expression during the Tetrahymena thermophila life cycle. PLoS ONE *4*, e4429.

97. Xiong, J., Yuan, D., Fillingham, J.S., Garg, J., Lu, X., Chang, Y., Liu, Y., Fu, C., Pearlman, R.E., and Miao, W. (2011). Gene network landscape of the ciliate Tetrahymena thermophila. PLoS ONE *6*, e20124.

98. Mochizuki, K. (2008). High efficiency transformation of Tetrahymena using a codon-optimized neomycin resistance gene. Gene *425*, 79–83.

99. Yao, M.C., and Yao, C.H. (1991). Transformation of Tetrahymena to cycloheximide resistance with a ribosomal protein gene through sequence replacement. Proc. Natl. Acad. Sci. USA *88*, 9493–9497.

100. Shang, Y., Song, X., Bowen, J., Corstanje, R., Gao, Y., Gaertig, J., and Gorovsky, M.A. (2002). A robust inducible-repressible promoter greatly facilitates gene knockouts, conditional expression, and overexpression of homologous and heterologous genes in Tetrahymena thermophila. Proc. Natl. Acad. Sci. USA *99*, 3734–3739.

101. Chilcoat, N.D., Melia, S.M., Haddad, A., and Turkewitz, A.P. (1996). Granule lattice protein 1 (Grl1p), an acidic, calcium-binding protein in Tetrahymena thermophila dense-core secretory granules, influences granule size, shape, content organization, and release but not protein sorting or condensation. J. Cell Biol. *135*, 1775–1787.

102. Cassidy-Hanley, D., Bowen, J., Lee, J.H., Cole, E., VerPlank, L.A., Gaertig, J., Gorovsky, M.A., and Bruns, P.J. (1997). Germline and somatic transformation of mating Tetrahymena thermophila by particle bombardment. Genetics *146*, 135–147.

103. Iwamoto, M., Koujin, T., Osakada, H., Mori, C., Kojidani, T., Matsuda, A., Asakawa, H., Hiraoka, Y., and Haraguchi, T. (2015). Biased assembly of the nuclear pore complex is required for somatic and germline nuclear differentiation in Tetrahymena. J. Cell Sci. *128*, 1812–1823.

104. Haraguchi, T., Kojidani, T., Koujin, T., Shimi, T., Osakada, H., Mori, C., Yamamoto, A., and Hiraoka, Y. (2008). Live cell imaging and electron microscopy reveal dynamic processes of BAF-directed nuclear envelope assembly. J. Cell Sci. *121*, 2540–2554.

105. Bolte, S., and Cordelières, F.P. (2006). A guided tour into subcellular colocalization analysis in light microscopy. J. Microsc. *224*, 213–232.

STAR★METHODS

KEY RESOURCES TABLE

REAGENT or RESOURCE	SOURCE	IDENTIFIER
Antibodies		
mouse monoclonal anti-Grl3p (5E9)	Turkewitz's lab [82]	N/A
mouse monoclonal anti-Grt1p (4D11)	Turkewitz's lab [46]	N/A
rabbit polyclonal anti-Grl1p	Turkewitz's lab [83]	N/A
rabbit polyclonal anti-GFP	Invitrogen	Cat#A11122
Texas-Red-conjugated goat anti-mouse	Invitrogen	Cat#T6390
Alexa 488-conjugated donkey anti-rabbit	Invitrogen	Cat#A21206
mouse monoclonal anti-GFP	BioLegend	Cat#MMS-118P-200
mouse monoclonal anti-c-myc (9E10)	Sigma Aldrich	Cat#M4439
rabbit anti-FLAG	Sigma Aldrich	Cat#F7425
mouse anti-HA (HA.11)	BioLegend	Cat#MMS-101P
anti-rabbit IgG (whole molecule)-HPeroxidase	Sigma Aldrich	Cat#022M4811
Horseradish Peroxidase-linked anti-mouse	GE Healthcare Life Sciences	Cat#NA931
EZ view Red Anti-FLAG M2 Affinity Gel	Sigma Aldrich	Cat#F2426
Pierce Anti-c-Myc Agarose	Thermo Fisher Scientific	Cat#20168
GFP-nAb agarose Spin Kit	Allele Biotechnology	Cat# ABP-nAb-GFPAK20
DyLight 488	Thermo Fisher Scientific	Cat#1860501
DyLight 650	Thermo Fisher Scientific	Cat#1862393
Chemicals, Peptides, and Recombinant Proteins		
1-Methyl-3-nitro-1-nitrosoguanidine	Sigma Aldrich	Cat#129941
Alcian Blue 8GX	Sigma Aldrich	Cat#A5268
Dibucaine hydrochloride	Sigma Aldrich	Cat#D0638
Paromomycin sulfate salt	Sigma Aldrich	Cat#P5057
Cycloheximide	Sigma Aldrich	Cat#C1988
Blasticidin S HCL	Research Products International	Cat#B12200
Cadmium chloride	Sigma Aldrich	Cat#C3141
FM4-64	Invitrogen	Cat#T3166
Lysotracker	Life Technologies	Cat#L7528
Paraformaldehyde	Sigma Aldrich	Cat#P6148
Low melting temperature agarose (SeaPlaque Agarose)	Lonza	Cat#50101
Osmium tetroxide	Nisshin EM	Cat#3002
Uranyl acetate dehydrate	Wako	Cat#554-85072
EPON	Nisshin EM	Cat#3402
Lead citrate	Sigma Aldrich	Cat#18-0875-2
Poly(ethylene oxide)	Sigma Aldrich	Cat#189456
Glutaraldehyde solution 50%	Sigma Aldrich	Cat#340855
Roche mini complete EDTA free	Roche	Cat#11836170001
SuperSignal West Femto Maximum Sensitivity Substrate	Thermo Fisher Scientific	Cat #34095
BSA	Thermo Fisher Scientific	Cat#BP1600
Instant Nonfat Dry Milk	Quality Biological, Inc	Cat#A614-1005
Osmium tetroxide 4% (EM)	Electron Microscopy Science	Cat#19150
Tween 20	Sigma Aldrich	Cat#P2287
Bacto Proteose peptone	BD Biosciences	Cat#211684
Bacto Yeast extract	BD Biosciences	Cat#212750
D(+)-Glucose	ACROS Organics	Cat#41095-0010

(*Continued on next page*)

Continued

REAGENT or RESOURCE	SOURCE	IDENTIFIER
Ethylenediaminetetraacetic acid ferric sodium salt	Sigma Aldrich	Cat#E6760
Penicillin G sodium salt	Sigma Aldrich	Cat#P3032
Streptomycin sulfate	MP BIOMEDICALS	Cat#02100556
Amphotericin B fungizone	USBiological, Life Sciences	Cat#A2230
Deposited Data		
T. thermophila protein sequences used to construct the phylogenetic tree in Figures 6A and S4A	http://ciliate.org/index.php/home/welcome	N/A
T. malaccensis protein sequences used to construct the phylogenetic tree in Figures 6A and S4A	http://ciliate.org/index.php/home/welcome	N/A
P. tetraurelia protein sequences used to construct the phylogenetic tree in Figures 6A and S4A	http://paramecium.cgm.cnrs-gif.fr/	N/A
P. caudatum protein sequences used to construct the phylogenetic tree in Figures 6A and S4A	http://paramecium.cgm.cnrs-gif.fr/	N/A
S. coeruleus protein sequences used to construct the phylogenetic tree in Figure 6A	http://stentor.ciliate.org/index.php/home/welcome	N/A
O. trifallax protein sequences used to construct the phylogenetic tree in Figure 6A	http://oxy.ciliate.org/index.php/home/welcome	N/A
S. lemnae protein sequences used to construct the phylogenetic tree in Figure 6A	http://stylo.ciliate.org/index.php/home/welcome	N/A
I. multifiliis protein sequences used to construct the phylogenetic tree in Figure 6A	http://ich.ciliate.org/index.php/home/welcome	N/A
M. fuscus, BankIt2082687 contig-19132000004_Vps39, sequence used to construct the phylogenetic tree in Figure 6A	GenBank	MG896212
M. fuscus, BankIt2082687 contig-2809000003_Vps3, sequence used to construct the phylogenetic tree in Figure 6A	GenBank	MG896213
M. fuscus, BankIt2082687 contig-12000001_Vps8, sequence used to construct the phylogenetic tree in Figure 6A	GenBank	MG896214
M. fuscus, BankIt2082687 contig-1059000002_Vps33, sequence used to construct the phylogenetic tree in Figure 6A	GenBank	MG896215
M. fuscus, BankIt2082687 contig-411000004_Vps18, sequence used to construct the phylogenetic tree in Figure 6A	GenBank	MG896216
M. fuscus, BankIt2082687 contig-428000003_Vps11, sequence used to construct the phylogenetic tree in Figure 6A	GenBank	MG896217
M. fuscus, BankIt2082687 contig-3173000000_Vps16, sequence used to construct the phylogenetic tree in Figure 6A	GenBank	MG896218
Experimental Models: Organisms/Strains		
CU428.1	*Tetrahymena* stock center, Cornell University	N/A
UC616	This paper	N/A
Cth3p-GFP	[81]	N/A
Sor4p-GFP	[47]	N/A
Grl3p-GFP	[48]	N/A
Igr1p-GFP	[82]	N/A
Stx7l1p-GFP	[48]	N/A
mCherry-Rab7p	This paper	N/A
mCherry-Rab22Ap	This paper	N/A
Δvps8a	This paper	N/A
Δvps8b	This paper	N/A
Δvps8e	This paper	N/A
Δvps8f	This paper	N/A
Δvps8a/Grl3p-GFP	This paper	N/A
Δvps8a/Sor4p-GFP	This paper	N/A

(*Continued on next page*)

Continued

REAGENT or RESOURCE	SOURCE	IDENTIFIER
Δvps8a/Cth3p-GFP	This paper	N/A
Δvps8a/Igr1p-GFP	This paper	N/A
Δvps8a/Stx7l1p-GFP	This paper	N/A
Δvps8a/mCherry-Rab7p	This paper	N/A
Δvps8a/mCherry-Rab22Ap	This paper	N/A
UC616/Vps8ap-GFP	This paper	N/A
SB281/Vps8ap-GFP	This paper	N/A
Vps8ap-mNeon	This paper	N/A
Vps8ap-FF-ZZ	This paper	N/A
Vps8ap-mNeon/mCherry-Rab7p	This paper	N/A
Vps8ap-mNeon/mCherry-Rab22Ap	This paper	N/A
Vps8ap-FF-ZZ/Vps16ap-HA	This paper	N/A
Vps8ap-FF-ZZ/Vps16bp-HA	This paper	N/A
Vps16ap-HA	This paper	N/A
Vps16bp-HA	This paper	N/A
Vps8ap-FF-ZZ/c-myc-Rab7p	This paper	N/A
Vps8ap-FF-ZZ/c-myc-Rab22Ap	This paper	N/A
Vps8ap-mNeon/Sor4p-mCherry	This paper	N/A
Sor4p-GFP/mCherry-Rab7p	This paper	N/A
Δvps8a/Sor4p-GFP/mCherry-Rab7p	This paper	N/A
Oligonucleotides		
00290710_fw, to test intron retention by RT-PCR: ctcttaatgcacatgtattc tagtcttac	This paper	N/A
00290710_rev, to test intron retention by RT-PCR: atttcccactataatatct cgccttcta	This paper	N/A
Btu1_F, used as housekeeping gene for RT-PCR: atgagagaaatcgttcacatc	This paper	N/A
Btu1_R, used as housekeeping gene for RT-PCR: tgaccgaaaacgaagttatc	This paper	N/A
inf00290710_fw, inf00290710_fw, to construct pVPS8A-mEGFP_neo4: atgcgctagcggatcctatgaatcaagttaaaaatctcc	This paper	N/A
inf00290710_rv, to construct pVPS8A-mEGFP_neo4: tagaaaccatggat ccttcaaaaaaatttagctattcag	This paper	N/A
3′UTRvps8_inf_fw, to construct pVPS8A-mEGFP_neo4: ggatctgaattcg atatcttgtgaatctaaaataatattttc	This paper	N/A
3′UTRvps8_inf_rv, to construct pVPS8A-mEGFP_neo4: atcgataagcttgat atctaagacttctttttgattatcg	This paper	N/A
5′UTR_VPS8_NheI_fw, to construct pVPS8AMACKO-Neo4: ctagctag catatattcgttaataatttaactattg	This paper	N/A
5′UTR_VPS8_Pst1_rev, to construct pVPS8AMACKO-Neo4: aaactgc agaactaactacagctatctttttttggc	This paper	N/A
N/A5′UTR_VPS8.2_sacI_FW, to construct pVPS8BMACKO-Neo4: tccag agctcgccgagcggtctaaggcggcgcact	This paper	N/A
5′UTR_VPS8.2_pstI_REV, to construct pVPS8BMACKO-Neo4: aaaac tgcagtgaaaatctcagccttaacagcaagc	This paper	N/A
3′UTR_VPS8.2_xho_FW, to construct pVPS8BMACKO-Neo4: ccgctcg aggtattttaataaattttgaattatttca	This paper	N/A
3′UTR_VPS8.2_apa_REV, to construct pVPS8BMACKO-Neo4: ttaatggg cccttcaattctaacactctttcttaagt	This paper	N/A
5′UTR_VPS8.3_sacI_FW, to construct pVPS8CMACKO-Neo4: tccagagctc actaaaaattcacattattttgaaat	This paper	N/A
5′UTR_VPS8.3_pstI_REV, to construct pVPS8CMACKO-Neo4: aaaactg cagtcactttaaaattattaaattatatc	This paper	N/A

(*Continued on next page*)

Continued

REAGENT or RESOURCE	SOURCE	IDENTIFIER
3′UTR_VPS8.3_xho_fw, to construct pVPS8CMACKO-Neo4: ccgctcgagcaa actaaaagtattaacaagaaat	This paper	N/A
3′UTR_VPS8.3_apa_REV, to construct pVPS8CMACKO-Neo4: ttaatgggccc tttaagtacaaacctacaaatccaag	This paper	N/A
5′UTR_VPS8.4_sacI_FW, to construct pVPS8DMACKO-Neo4: tccagagctca tcattaaaactttatctattaat	This paper	N/A
5′UTR_VPS8.4_pstI_REV, to construct pVPS8DMACKO-Neo4: aaaactgc agttatttttagtatttgataaagttc	This paper	N/A
3′UTR_VPS8.4_xho_FW, to construct pVPS8DMACKO-Neo4: ccgctcgagc aagcttttatagatttaatttaaatg	This paper	N/A
3′UTR_VPS8.4_apa_REV, to construct pVPS8DMACKO-Neo4: ttaatgggc cccgatttatggtgaaactgatgaaag	This paper	N/A
5′ UTR_VPS8.5_NheI_fw, to construct pVPS8EMACKO-Neo4: aaagctagctaagaccaactaatattaaataaaact	This paper	N/A
5′UTR_VPS8.5_PstI_rev, to construct pVPS8EMACKO-Neo4: aaactgcagtttgatcttttaaatcttgtaatat	This paper	N/A
3′UTR_VPS8.5_EcorV_fw, to construct pVPS8EMACKO-Neo4: aaagatatcaagttgtaaattacaataaaaaattaat	This paper	N/A
3′UTR_VPS8.5_xhoI_rev, to construct pVPS8EMACKO-Neo4: aaactcgagagaaattcctttataattttgtaat	This paper	N/A
5′UTR_VPS8.6_NheI_fw, to construct pVPS8FMACKO-Neo4: aaagctagccaatatttcattcttttaacttgaaaat	This paper	N/A
5′UTR_VPS8.6_PstI_rev, to construct pVPS8FMACKO-Neo4: aaactgcagctcttgatttttgctttattcagtatc	This paper	N/A
3′UTR_VPS8.6_EcorV_fw, to construct pVPS8FMACKO-Neo4: aaagatatcataagtaacaaattttattgagaaat	This paper	N/A
3′UTR_VPS8.6_XhoI_rev, to construct pVPS8FMACKO-Neo4: aaactcgagatgtaatcatattatttttttatataagt	This paper	N/A
00290710_RT_rev, to test the VPS8A locus by RT-PCR: gattcac aaaaaatttttattttaaaaaaatc	This paper	N/A
00290710_seq4_fw, to test the VPS8A locus by RT-PCR: cttattgt tcagattgtgataaaag	This paper	N/A
RT_VPS8.2_fw, to test the VPS8B locus by RT-PCR: accaaaaattt gccaaatcgtttaaact	This paper	N/A
VPS8.2stopTOPO_rev, to test the VPS8B locus by RT-PCR: tcattg ttgagaatagatataatcttatgt	This paper	N/A
RT_VPS8.3_fw, to test the VPS8C locus by RT-PCR: gcttaaagtatac aaagggtcttcaaag	This paper	N/A
VPS8.3stop_TOPO_rev, to test the VPS8C locus by RT-PCR: tcaat acaaatcagtaacctcttcaaatatg	This paper	N/A
RT_VPS8.4_fw, to test the VPS8D locus by RT-PCR: atacagagcaa gatctaaattcttaaat	This paper	N/A
VPS8.4_RT_rev, to test the VPS8D locus by RT-PCR: tcatttaaattaaat ctataaaagcttgga	This paper	N/A
RT_KO_VPS8.5_fw, to test the VPS8E locus by RT-PCR: tttaagtttgagca ggaacaatagctact	This paper	N/A
RT_KO_VPS8.5_rev, to test the VPS8E locus by RT-PCR: attaatttttt attgtaatttacaacttttt	This paper	N/A
RT_KO_VPS8.6_fw, to test the VPS8F locus by RT-PCR: gtcacacagt agaataaatgaaaaaacct	This paper	N/A
RT_KO_VPS8.6_rev, to test the VPS8F locus by RT-PCR: aaataatttct caataaaatttgttacttataatt	This paper	N/A
2xmneon_inf_fw, to construct p2mNeon-6myc-Neo4: ccgctctagaacta gttgtccgcgacgcgtaatg	This paper	N/A

(*Continued on next page*)

Continued

REAGENT or RESOURCE	SOURCE	IDENTIFIER
2xmneon_inf_rv, to construct p2mNeon-6myc-Neo4: agttcgctcaactag ttcccgggctgcaggaatt	This paper	N/A
CHXcassette_PstI_F, to construct pSOR4-mEGFP-Chx: gggctgcagact atttaagtcagtagaattttag	This paper	N/A
CHXcassette_EcorV_R, to construct pSOR4-mEGFP-Chx: aaagatatc gggctgcatttttccagtaaaaatttg	This paper	N/A
5′_CTH3_sacI_fw, to construct pCTH3-mEGFP-Chx: ctagagctcttggctttc ccttctatggctgcct	This paper	N/A
5′_CTH3_bamHI_rev, to construct pCTH3-mEGFP-Chx: cagggatccat gtcttgccaaagcaaaaccaact	This paper	N/A
3′UTR_CTH3_ecorV_fw, to construct pCTH3-mEGFP-Chx: aaagatatcg atagttattacagtcttgaatggga	This paper	N/A
3′UTR_CTH3_xho_rev, to construct pCTH3-mEGFP-Chx: aaactcgagcaatta cttatttgttattttggcttgt	This paper	N/A
5′VPS8_SacI_fw, to construct pVPS8A-2mNeon-6myc-Neo4: ctagagct ctacaaagaatagaacagaatatacct	This paper	N/A
5′VPS8_MluI_rev, to construct pVPS8A-2mNeon-6myc-Neo4: attacgcg tcgttcaaaaaaatttagctattcag	This paper	N/A
ZZ flag_MluI_fw, to construct pVPS8A-FF-ZZ-Neo4: aaaacgcgtaggatc cgattacaaagatcatgatggt	This paper	N/A
ZZflag_spel_rev, to construct pVPS8A-FF-ZZ-Neo4: cagttcgctcaacta gtattagcatcaaccttag	This paper	N/A
HA_PmeIMluI_fw, to construct 2HA-ncvb: aaagtttaaacacgcgtagcggta gttatccttacgac	This paper	N/A
HA_apa_rev, to construct 2HA-ncvb: aaaagggccctcaactagtcgcataatccgga	This paper	N/A
VPS16a_FW, to construct pVPS16A-2HA-ncvb: aagtttaaacacgcgtatgg aagattcattaattttaca	This paper	N/A
VPS16a_RV, to construct pVPS16A-2HA-ncvb: aactaccgctacgcgtacgca tgttataaattgattaag	This paper	N/A
VPS16b_FW, to construct pVPS16B-2HA-ncvb: aagtttaaacacgcgtatga tatttcacgaagatattat	This paper	N/A
VPS16b_RV, to construct pVPS16B-2HA-ncvb: aactaccgctacgcgttttt ctaagaccagctgatta	This paper	N/A
Rab7_Q/L_NheIF, to construct p2HA-3mCherry-RAB7-ncvb: ctagctagc atgagcacaaataaaagaaagcaac	This paper	N/A
Rab7_Q/L_ApaIR, to construct p2HA-3mCherry-RAB7-ncvb: ttgggc cctcaacaagggcagtcatcc	This paper	N/A
Rab22A_Q/L_NheIF, to construct p2HA-3mCherry-RAB22A-ncvb: ctagc tagcatgtacgcagaagaaattaaagttgtc	This paper	N/A
Rab22A_Q/L_ApaIR, to construct p2HA-3mCherry-RAB22A-ncvb: ttgggc cctcaacaggggcaagatcc	This paper	N/A
2X HA tag (PmeI)F, to construct p2HA-3mCherry-RAB7/RAB22A-ncvb: agctttgtttaaacatgtatccttacgacgttcctgattatgctggttatccatacgatgttccgga ttatgcgggtagtatggattcaacagaatcagg	This paper	N/A
mCherryXbaI_F, to construct p2HA-3mCherry-RAB7/RAB22A-ncvb: gctc tagaatggattcaacagaatcaggaag	This paper	N/A
NewmCherryNheI_R, to construct p2HA-3mCherry-RAB7/RAB22A-ncvb: gatgctagcagatgagctgcttcctgatg	This paper	N/A
Linker_nhel_fw2, to construct pSOR4_3mCherry2HA_Chx: caacggctagcggat ctcaaggatcatcaggaagc	This paper	N/A
mCherry_spel_rev, to construct pSOR4_3mCherry2HA_Chx: gagatccacta gttttgtaaagttcatccatac	This paper	N/A
5′ SOR4_sacI_fw, to construct pSOR4_3mCherry2HA_Chx: ctggagctcg ttggtgatttaagaatggtctaag	This paper	N/A

(*Continued on next page*)

Continued

REAGENT or RESOURCE	SOURCE	IDENTIFIER
5′SOR4_NheI_inf_RV, to construct pSOR4_3mCherry2HA_Chx: cttgagat ccgctagcaagcatatctgcatcgtattc	This paper	N/A
5utrRab22A_sacI_fw, to construct p6_c-myc_RAB22A_Chx: aaagagctc ttttgcaaacaagttaaccttgact	This paper	N/A
5utrRab22A_bamHI_rev, to construct p6_c-myc_RAB22A_Chx: aaaggatc ctgataatcagtatatacttattctttaag	This paper	N/A
3utrRab22A_xho_fw, to construct p6_c-myc_RAB22A_Chx: aaactcgagagga acttttttaatatatgggatta	This paper	N/A
3utrRab22A_kpnI_rev, to construct p6_c-myc_RAB22A_Chx: aaaggtac cattcatataatcaataaacaaattagt	This paper	N/A
Rab22A_inf_fw, to construct p6_c-myc_RAB22A_Chx: cagcccgggaac tagtatgtacgcagaagaaattaaagttg	This paper	N/A
Rab22A_inf_rev, to construct p6_c-myc_RAB22A_Chx: agttcgctcaactag ttcaacaggggcaagatcc	This paper	N/A
5utrRab7_sacI_fw, to construct p6_c-myc_RAB7_Chx: aaagagctcagaaaac aaatttcgaaacaaatact	This paper	N/A
5utrRab7_bamH1_rev, to construct p6_c-myc_RAB7_Chx: aaaggatccta cttaagtaaatttatttttttgtttttaac	This paper	N/A
3utrRab7_xho_fw, to construct p6_c-myc_RAB7_Chx: aaactcgagttgagaa aaatgaaagcatctgac	This paper	N/A
3utrRab7_kpn1_rev, to construct p6_c-myc_RAB7_Chx: tctacatggtaccctta taaattgagatg	This paper	N/A
Rab7_inf_fw, to construct p6_c-myc_RAB7_Chx: cagcccgggaactagtatgagc acaaataaaagaaagcaac	This paper	N/A
Rab7_inf_rev, to construct p6_c-myc_RAB7_Chx: agttcgctcaactagttcaa caagggcagtcatcc	This paper	N/A
6myc_bamH1_fw, to construct p6_c-myc_RAB7/RAB22A_Chx: catgcgg atccgtacggtatcgatttaaagctatg	This paper	N/A
6myc_ speI_rev, to construct p6_c-myc_RAB7/RAB22A_Chx: gctcaacta gttcccgggctgcaggaattca	This paper	N/A
1xmcherry2xHA, to construct pSOR4_3mCherry2HA_Chx: tggcggccgctct agagctagcggatctcaaggatcatcaggaagcagctcatctgctagaatggattcaacagaatc aggaagcacagaatcagttattaaagaatttatgagatttaaggttcatatggaaggttctgttaacgg tcacgaatttgaaattgaaggagaaggagaaggtagaccttatgaaggaacacaaactgctaaat taaaagtaactaaaggtggtcctttacctttcgcatgggatattctttcacctcaatttatgtatggttct aaagcatatgttaaacaccctgctgatattcctgattatttaaagttgtcttttcctgaaggttttaagtg ggaaagagttatgaatttgaagatggtggagttgttacagtaactcaagattcttctttacaagatgg agaatttatttataaagttaaattaagaggtactaattttcctagcgatggacctgtcatgcaaaaga aaacaatgggttgggaagcaagttctgaaagaatgtaccctgaagatggtgcacttaaaggaga aattaagcaaagattaaaacttaaagatggtggacattatgatgctgaagtcaaaactacttataaa gcaaagaaacctgttcaattacctggtgcatacaatgttaatattaagttagatattacatctcataa tgaagattacacaatagtagaacaatacgaaagagctgaaggtagacacagtactggtggta tggatgaactttacaaaactagcggtagttatccttacgacgttcctgattatgctggttatcca tacgatgttccggattatgcgactagttgatctagagcatgcgcta	This paper	N/A
Recombinant DNA		
pVPS8A-mEGFP_neo4	This paper	N/A
pSOR4-mEGFP-Chx	This paper	N/A
pSOR4_3mCherry2HA_Chx	This paper	N/A
pCTH3-mEGFP-Chx	This paper	N/A
pGRL3-smGFP-2myc-6His-Chx	[48]	N/A
pVPS8A-2mNeon-6myc-Neo4	This paper	N/A
p2mNeon-6myc-Neo4	This paper	N/A
pVPS8A-FF-ZZ-Neo4	This paper	N/A
pVPS16A-2HA-ncvb	This paper	N/A

(*Continued on next page*)

Continued

REAGENT or RESOURCE	SOURCE	IDENTIFIER
pVPS16B-2HA-ncvb	This paper	N/A
p6_c-myc_RAB7_Chx	This paper	N/A
p6_c-myc_RAB22A_Chx	This paper	N/A
p2HA-3mCherry-RAB7-ncvb	This paper	N/A
p2HA-3mCherry-RAB22A-ncvb	This paper	N/A
IGR1-mEGFP-ncvb	[82]	N/A
STX7L1-mEGFP-ncvb	[48]	N/A
pVPS8AMACKO-Neo4	This paper	N/A
pVPS8BMACKO-Neo4	This paper	N/A
pVPS8CMACKO-Neo4	This paper	N/A
pVPS8DMACKO-Neo4	This paper	N/A
pVPS8EMACKO-Neo4	This paper	N/A
pVPS8FMACKO-Neo4	This paper	N/A
Software and Algorithms		
Picard Tools version 1.111	Broad Institute	N/A
Zen 2.1 software	Zeiss	N/A
Slidebook 6 software	Zeiss	N/A
Burrows-Wheeler Aligner software (BWA) version 0.7.10	[84]	N/A
Genome Analysis Toolkit (GATK) version 3.3.0	[85]	N/A
Fiji	[86]	N/A
Huygens Professional	Scientific Volume Imaging	N/A
BLAST suite	[87]	N/A
CIPRES	[88]	N/A
RaxML version 8.2.10	[89]	N/A
MrBayes version 3.2.6	[90]	N/A
MUltiple Sequence Comparison by Log-Expectation tool (MUSCLE) version 3.8.31	[91]	N/A
ProtTest 3	[92]	N/A
Other		
nProtein A Sepharose 4 Fast Flow resin	GE Healthcare Life Sciences	Cat #GE17-5280-01
Novex 4-20% Tris-Glycine Mini Gels, WedgeWell format	Invitrogen	*Cat #XP04200BOX*
PVDF Transfer Membrane, 0.2 μm, 26.5 cm x 3.75 m	Thermo Fisher Scientific	*Cat #88520*
NuPAGE LDS Sample Buffer (4X)	Invitrogen	*Cat #NP0007*
Novex Tris-Glycine SDS Running Buffer (10X)	Invitrogen	Cat #LC2675
Novex Tris-Glycine Transfer Buffer (25X)	Invitrogen	Cat #LC3675

CONTACT FOR REAGENT AND RESOURCE SHARING

Further information and requests for resources and reagents should be directed to and will be fulfilled by the Lead Contact, Aaron P. Turkewitz (apturkew@uchicago.edu).

EXPERIMENTAL MODEL AND SUBJECT DETAILS

Cell strains and culture conditions

Tetrahymena thermophila strains used in this work are indicated in the Key Resources Table, and in Table S3. Cells were grown overnight in SPP (2% proteose peptone, 0.1% yeast extract, 0.2% dextrose, 0.003% ferric-EDTA) supplemented with 250 ug/ml penicillin G, 250 ug/ml streptomycin sulfate, and 0.25 μg/ml amphotericin B fungizone, to medium density (1-3 × 10^5 cells/ml). For biolistic transformation, growing cells were subsequently starved in 10 mM Tris buffer, pH 7.4. Fed and starved cells were both kept at 30°C with agitation at 99 rpm. For live microscopy, grown cells were transferred to S medium (0.2% yeast extract, 0.003% ferric-EDTA) for 2-4 hours prior to imaging. Culture densities were measured using a Z1 Coulter Counter (Beckman Coulter Inc.).

METHOD DETAILS

Genetic methods

The methods used for genetic crosses, selecting progeny, and mating type determination are as previously detailed [50].

Testing assortants for exocytosis competence

Assortants were tested for the ability to secrete mucocysts in response to the secretagogue Alcian blue, using a 96-well plate format and subsequently in bulk cultures, as described previously [50].

Genomic DNA extraction

Genomic DNA was extracted as previously described [50]. In brief, cells were grown to $3x10^5$ cells/ml in 25 mL SPP, and starved for 18–24h in 10 mM Tris-HCl, pH 7.5; 1.5 mL of cells was then concentrated to 50 μL by low-speed centrifugation, dissolved in 700 μL urea buffer (42% w/v urea, 0.35 M NaCl, 0.01 M Tris pH 7.4, 0.01 M EDTA, 1% SDS) with 0.1 mg/ml Proteinase K by gentle shaking for 5 min at 50°C. The fraction containing genomic DNA was then isolated with 750 μL phenol:chloroform:isoamyl alcohol (25:24:1), and the top layer was then extracted with an equal volume of chloroform: isoamyl alcohol (24:1), and mixed with a one-third volume of 5 M NaCl. The DNA was precipitated with an equal volume of isopropyl alcohol, washed and pelleted twice with 1 mL 70% ethanol. The DNA pellet was resuspended in 25 μL TE, pH 8.0, treated with 2 μL RNase A (10 mg/ml, Fermentas) overnight at 55°C, and stored at –20°C.

Whole genome sequencing

The genome sequencing of the F2 pools was performed as previously described [50]. A total number of 295 million paired-end reads (2 X 100 bp) were generated. The F2 lines with the mutation (UC616) of interest were sequenced to ~147-fold genome coverage. The F2 lines showed the wild-type phenotype (WT) were sequenced to ~180-fold genome coverage. Strain SB281 was sequenced to ~198-fold genome coverage. Summary of UC616 and SB281 genome DNA sequencing data is shown in Table S4. Genome sequencing of *Tetrahymena* primarily reflects the Macronuclear genome in which genes are generally present at ~45 copies, compared to the two copies in the Micronucleus. Because the Micronucleus represents the germline nucleus, only Micronuclear alleles are transmitted to progeny [93]. However, because all parental lines are wild-type for exocytosis except for UC616 itself, we made the simplifying assumption that bulk DNA sequencing of phenotypically mutant versus wild-type F2 lines would identify the UC616 causative mutation.

Sequence alignment

For the analysis of the sequenced genomes, reads from total genomic DNA sequencing were mapped to the *T. thermophila* Macronuclear genome sequence released by Broad Institute using the Burrows-Wheeler Aligner software (BWA) version 0.7.10 [84, 94, 95]. Default parameters were used when running bwa mem except the following: 1) Adding proper read group IDs for each sample; 2) Enabling ''Mark shorter split hits as secondary'' using the –M option. The output files were sorted by coordinates and converted to bam files using the Picard Tools version 1.111. Picard Tools was also used to remove PCR duplicates and index the bam files. To align the *VPS8A* genomic region (TGD: TTHERM_00290710, http://ciliate.org), containing the identified SNV, and the corresponding transcript (TFGD: TranscriptID_000003408, http://tfgd.ihb.ac.cn/), we used MUltiple Sequence Comparison by Log- Expectation tool (MUSCLE) version 3.8.31.

Variant discovery

The Genome Analysis Toolkit (GATK) version 3.3.0 was applied to identify variants with total genomic DNA sequencing data of the three samples [85]. The following steps were taken in this procedure. 1) Realignment of reads using ''RealignerTargetCreator'' and ''IndelRealigner'' tool to correct the misalignment caused by site mutations, insertions and deletions; 2) haplotypes of each sample were called using the ''HaplotypeCaller'' tool with the ''emitRefConfidence'' set to ''GVCF,'' ''variant_index_type'' set to ''LINEAR,'' ''variant_index_parameter'' set to ''128000,'' ''genotyping_mode'' set to ''DISCOVERY,'' ''stand_emit_conf'' set to ''10,'' and ''stand_call_conf'' set to ''30''; and 3) variances in the three samples were jointly called using the ''GenotypeGVCFs'' tool. Full documentation of parameters can be found at https://www.broadinstitute.org/gatk/guide/tooldocs/org_broadinstitute_gatk_tools_walkers_haplotypecaller_HaplotypeCaller.php#-output_mode. A total number of 51,121 variants was called with this procedure. Among these, 31,744 were Single Nucleotide Variants (SNVs), which resulted in an SNV density of ~0.31 kbp^{-1} for a genome of a mappable size of 103,014,375 bp [94].

Candidate screening

The candidate causal variants of the exocytosis deficient phenotype were selected as previously described [50]. A total of 35 such candidate sites was found in UC616. Among these 35 SNVs, 10 lay within coding regions or at intron-exon junctions.

Transcription profiles

Gene expression profiles were downloaded from the *Tetrahymena* Functional Genomics Database (TFGD, http://tfgd.ihb.ac.cn/) [96, 97]. For plotting the graphs, each profile was normalized by setting the gene's maximum expression level to 1.

Generation of VPS8 knockout strains

The Macronuclear open reading frame (ORF) of each of the *VPS8* paralogs (TTHERM_00290710, *VPS8A*; TTHERM_00393150, *VPS8B*; TTHERM_00716100, *VPS8C*; TTHERM_00532700, *VPS8D*; TTHERM_00691590, *VPS8E*; TTHERM_00384890, *VPS8F*) was replaced with the paromomycin (Neo4) drug resistance cassette [98] via homologous recombination with the linearized vectors pVPS8AMACKO-Neo4, pVPS8BMACKO-Neo4, pVPS8CMACKO-Neo4, pVPS8DMACKO-Neo4, pVPS8EMACKO-Neo4, pVPS8FMACKO-Neo4. PCR was used to amplify 500-800bp of the genomic regions upstream (5′UTR) and downstream (3′UTR) of each ORF. The amplified fragments were subsequently cloned into specific restriction sites, flanking the Neo4 cassette of the pNeo4 vector, by Quick Ligation (New England, Biolabs Inc.) unless otherwise specified: NheI/PstI and EcoRV sites for TTHERM_00290710 [the 3′UTR was introduced in the linearized pNeo4 vector by In-Fusion cloning kit (Clontech, Mountain View, CA), at the EcoRV site]; SacI/PstI and XhoI/ApaI sites for TTHERM_00393150, TTHERM_00716100, TTHERM_00532700; NheI/PstI and XhoI/EcoRV sites for TTHERM_00691590, TTHERM_00384890. The primers used to create these constructs are listed in the Key Resources Table. Each construct was linearized by digestion with SacI and KpnI and transformed into CU428.1 cells by biolistic transformation.

RT-PCR assessment of VPS8 disruption, and intron retention in the VPS8A transcript of UC616

$3x10^5$ cells from overnight cultures were pelleted, washed once with 10mM Tris, pH 7.4, and total RNA was isolated using RNeasy Mini Kit (QIAGEN, Valencia, CA) according to the manufacturer's instructions. The cDNA synthesis, from 2 μg of total RNA, was performed as per manufacturer's instructions using High-Capacity cDNA Reverse Transcription Kit (Applied Biosystems, Foster City, CA). The cDNA was PCR amplified to assay the presence of the corresponding transcripts (200-250bp) in the knockout strains, and the retention of the intron in the *VPS8A* transcript (250bp) of UC616 and SB281, using primers listed in the Key Resources Table. To confirm that equal amounts of cDNA were being amplified, reactions with primers specific for β-tubulin 1 (*BTU1*) were run in parallel.

Expression of Vps8ap-GFP in mutant strains

VPS8A was C-terminally fused to monomeric enhanced GFP (mEGFP), and reintroduced at the endogenous *VPS8A* locus in UC616 and SB281 by homologous recombination, using pVPS8A-mEGFP-Neo4. To rescue the *VPS8A* mutation in UC616 and SB281 by expressing a wild-type copy of the gene, 4352bp (of a total of 5091bp) of the *VPS8A* genomic sequence (minus the stop codon), were cloned in the linearized pmEGFP-Neo4 vector [47] at the BamH1 site, by In-Fusion cloning (Clontech, Mountain View, CA). The construct also contains 565bp of *VPS8A* downstream genomic sequence, following the Neo4 drug resistance cassette, cloned in the linearized vector at the EcoRV site, as described earlier for the pVPS8AMACKO-Neo4 vector. The construct was then linearized with NotI and KpnI, and introduced in the Macronucleus by biolistic transformation. The two *VPS8A* fragments were amplified by PCR with primers listed in the Key Resources Table.

Expression of Grl3p-GFP, Cth3p-GFP and Sor4p-GFP at the corresponding endogenous locus in *Δvps8a*

The pSOR4-mEGFP-Neo4 vector [47] was used as template to create pSOR4-mEGFP-Chx and pCTH3-mEGFP-Chx vectors. The former was obtained by replacing the Neo4 cassette in the pSOR4-mEGFP-Neo4 vector, with the cycloheximide (Chx) drug resistance cassette [99]. The Chx cassette was sub-cloned in the PstI and EcorV sites of the digested pSOR4-mEGFP vector. The pCTH3-mEGFP-Chx vector was created by replacing the 688bp and 625bp *SOR4* genomic fragments in the pSOR4-mEGFP-Chx construct, with the corresponding 817bp (minus the stop codon) and 710bp *CTH3* fragments, following digestion with SacI/BamHI and EcoRV/XhoI, respectively. All fragments were PCR amplified using primers listed in the Key Resources Table, and the sub-cloning was performed by Quick Ligation (New England, Biolabs Inc.). The pSOR4-mEGFP-Chx, pCTH3-mEGFP-Chx, and the previously-described pGRL3-smGFP-2myc-6His-Chx vectors [48], were linearized with SacI and KpnI, and transformed in *Δvps8a* by biolistic transformation.

Endogenous tagging of VPS8A with mNeon

Two mNeonGreen fluorescent tags were fused at the C terminus of the *VPS8A* macronuclear ORF via homologous recombination using linearized pVPS8A-2mNeon-6myc-Neo4. First, the p2mNeon-6myc-Neo4 vector was constructed. The 2xmNeon tag, followed by 6xc-myc tag, was PCR-amplified from pFAP256-mNeonGreen-6myc-BirA vector (a gift from J. Gaertig, University of Georgia, Athens, GA) and introduced at the SpeI site of a modified version of pNeo4, containing the *BTU1* terminator upstream of the Neo4 cassette, by In-Fusion cloning (Clontech, Mountain View, CA). The C-terminal 828 bp of the *VPS8A* genomic locus (lacking the stop codon) and, subsequently, the 565 bp-long downstream genomic region of *VPS8A*, were cloned at the SacI/MluI and EcoRV sites of the digested p2mNeon-6myc-Neo4 vector, respectively. The final vector was digested with SacI and KpnI prior to biolistic transformation of CU428.1. The primers are listed in the Key Resources Table.

Endogenous tagging of VPS8A with FF-ZZ tag

The FF-ZZ tag, containing 3xFLAG (FF), followed by the TEV (Tobacco Etch Virus cysteine protease) cleavage site and the IgG binding domain of protein A (ZZ-domain), was fused to the C terminus of *VPS8A* macronuclear ORF by homologous recombination, using pVPS8A-ZZflag-Neo4. The construct was obtained by PCR-amplifying the FF-ZZ tag from a donor vector, and subcloning it in the linearized pVPS8A-2mNeon-6myc-Neo4 vector at the MluI and SpeI sites, to replace the 2mNeon-6myc tag. The vec-

tor was linearized with SacI and KpnI prior to biolistic transformation of CU428.1. The primers are listed in the Key Resources Table.

Expression of Vps16ap-HA and Vps16bp-HA

Vps16ap-HA and Vps16bp-HA were integrated at the metallothionein 1 (*MTT1*) genomic locus [100] in CU428.1 and Vps8ap-FF-ZZ-expressing cell lines by homologous recombination, using VPS16ap-2HA-ncvb and VPS16bp-2HA-ncvb. The 2xHA tag was amplified from a donor vector and subcloned in the linearized ncvb vector at the PmeI and ApaI sites. The *VPS16A* and *VPS16B* ORFs were amplified from genomic DNA, and cloned in the linearized 2HA-ncvb by In-Fusion cloning (Clontech, Mountain View, CA) at the MluI site. The final constructs were linearized with SfiI and biolistically transformed in *Tetrahymena* strains. The primers are listed in the Key Resources Table.

Co-expression of Sor4p-mCherry, c-*myc*-Rab22Ap and c-*myc*-Rab7p with tagged Vps8ap

3xmCherry2xHA was fused to the C terminus of *SOR4* Macronuclear ORF via homologous recombination using linearized pSOR4_3mCherry2HA_Chx. The mCherry2xHA fragment was introduced into linearized pmEGFP-Neo4 by In-Fusion cloning (Clontech, Mountain View, CA) at the XbaI site, and the original mEGFP tag was removed by SpeI digestion followed by Quick Ligation (New England, Biolabs Inc.). Two additional mCherry tags were PCR-amplified and added at the NheI site of the linearized pmCherry2HA_Neo4 by compatible cohesive ends restriction cloning. The 3xmCherry2xHA tag was then subcloned in the linearized pSOR4_mEGFP_Chx vector at the SacI and SpeI sites. The C-terminal 694 bp of the *SOR4* genomic locus (lacking the stop codon) were PCR-amplified and re-introduced at the SacI/NheI site of the linearized pSOR4_3mCherry2HA_Chx. The final vector was digested with SacI and KpnI prior to biolistic transformation of Vps8ap-mNeon-expressing cell line.

6x c-*myc* was fused to the N terminus of Rab7p and Rab22Ap Macronuclear ORFs by homologous recombination, using p6_c-*myc*_Rab7_Chx and p6_c-*myc*_Rab22A_Chx, respectively. To construct p6_c-*myc*_Chx, 6x c-*myc* was PCR-amplified from a donor vector and subcloned in the linearized pmEGFP_Neo4 at the BamHI and SpeI sites. The Neo4 resistance cassette was then replaced with the Chx cassette by SpeI/HindIII digestion. *RAB7* or *RAB22A* Macronuclear ORFs were PCR-amplified and inserted by In-Fusion cloning (Clontech, Mountain View, CA) in the linearized p6 c-*myc*_Chx at the SpeI site. PCR was used to amplify 680-780bp of 5′ and 3′UTRs of *RAB7* and *RAB22A*. The 5′ and 3′UTR amplicons were cloned in the corresponding p6c-myc_Chx vector containing the appropriate *RAB* gene, by Quick Ligation (New England, Biolabs Inc.) at SacI/BamHI and XhoI/KpnI sites, respectively. The final vectors were digested with SacI and KpnI prior to biolistic transformation of Vps8ap-FF-ZZ-expressing cells. All primers are listed in the Key Resources Table.

Expression of mCherry-Rab7p, mCherry-Rab22Ap, Igr1p-GFP and Stx7l1p-GFP

mCherry-Rab7p, mCherry-Rab22Ap, Igr1p-GFP and Stx7l1p-GFP were integrated at the metallothionein 1 (*MTT1*) genomic locus in CU428.1 and *Δvps8a* strains by homologous recombination, using 2HA-3mCherry-RAB7-ncvb, 2HA-3mCherry-RAB22A-ncvb, and the previously described IGR1-mEGFP-ncvb [82] and STX7L1-mEGFP-ncvb [48] vectors. mCherry-Rab7p and mCherry-Rab22Ap were also transiently expressed in Vps8ap-mNeon expressing cell lines. In these constructs the transgene expression is under the control of the cadmium-inducible *MTT1* promoter [100]. The 2HA-mCherry tag was PCR-amplified and cloned in the PmeI/NheI sites of the p50 vector. Two additional mCherry tags were added at the NheI site of the linearized 2HA-mCherry-p50 by compatible cohesive ends restriction cloning. The 2HA3mCherry tag was then removed from the vector backbone by PmeI/NheI double digestion. The tag was joint to the N terminus of either *RAB7* or *RAB22A* Macronuclear ORFs by multiple fragment ligation. *RAB7* or *RAB22A* Macronuclear ORFs were previously PCR-amplified and NheI/ApaI digested, and introduced to the PmeI/ApaI-digested ncvb vector [46]. The 2HA-3mCherry-RAB7-ncvb,2HA-3mCherry-RAB22A-ncvb, IGR1-mEGFP-ncvb and STX7L1-mEGFP-ncvb constructs were linearized with SfiI and biolistically transformed into *Tetrahymena* strains. The primers are listed in the Key Resources Table.

Biolistic transformation

Tetrahymena transformants were generated and selected after biolistic transformation as previously described [48, 101, 102]. Transformants were serially transferred 6x/week in increasing concentrations of drug and decreasing concentrations of $CdCl_2$ (up to 1.2 mg/ml of paromomycin and 0.1 μg/ml $CdCl_2$; up to 18-20 μg/ml of cycloheximide and 0.5-1 μg/ml $CdCl_2$; up to 75-85 μg/ml of blasticidin and 0.1 μg/ml $CdCl_2$) for at least 3-5 weeks before further testing. At least three independent transformants were tested for each line.

Fluorescence and Immunofluorescence microscopy

Cells ($1.5x10^5$) were washed, fixed with 4% paraformaldehyde for 30 min, and immunolabeled as previously described [47, 52]. Grl3p and Grt1p were visualized using mouse mAbs (mAb) 5E9 (1:10) and 4D11 (1:4), respectively, followed by Texas Red-conjugated goat anti-mouse antibody (1:100) (Life Technologies, Carlsbad, CA). The simultaneous localization of Grt1p and Grl3p was performed as described earlier [47], by directly conjugating purified mAbs 4D11 and 5E9 to Dylight 488 and 650 (Thermo Scientific, Rockford, IL), respectively, and mixing them 1:1 before incubation with samples. For the simultaneous localization of Grl3p with either Igr1p-GFP or Stx7l1p-GFP, the expression of Igr1p-GFP and Stx7l1p-GFP was induced by incubating cells with $CdCl_2$ prior to the fixation. Samples were subsequently immunolabeled with 5E9 and Texas Red-conjugated anti-mouse IgG. Specifically, Igr1p-GFP-expressing

cells were treated with 1 μg/ml of $CdCl_2$ in SPP for 2h at 30°C, and then an additional 1 μg/ml of $CdCl_2$ was added for 2h. The expression of Stx7l1p-GFP was induced with 1 μg/ml of $CdCl_2$ for 3h at 30°C. For the simultaneous localization of Grl3p and Cth3p-GFP, cells were stained with 5E9 mAb and with rabbit polyclonal anti-GFP antibody (1:400) (Invitrogen), followed by incubation with Texas Red-conjugated goat anti-mouse and Alexa 488-conjugated donkey anti-rabbit antibodies (1:250) (Invitrogen), respectively, in 1% BSA blocking solution. The expression of mCherry-Rab7p or mCherry-Rab22Ap in wild-type, *Δvps8a*, and Vps8ap-mNeon-expressing cells, was induced with 1 μg/ml of $CdCl_2$ for 2.5h at 30°C prior to fixation. The visualization of Igr1p-GFP, Stx7l1p-GFP, Sor4p-GFP, Sor4p-mCherry, Vps8ap-mNeon, mCherry-Rab7p and mCherry-Rab22Ap in fixed cells was not enhanced with immunolabeling. Immunostained cells were mounted with Trolox (1:1000) to inhibit bleaching and imaged on a Zeiss LSM 880 Confocal Laser Scanning Microscope, 100X oil with NA = 1.4, with Zen2.1 software (Zeiss, Thornwood, NY). Fixed wild-type, *Δvps8a*, and Vps8ap-mNeon-expressing cells expressing, either mCherry-Rab7p or mCherry-Rab22Ap, or Sor4p-mCherry, were imaged on a Marianas Yokogawa type spinning disk inverted confocal microscope, 100X oil with NA = 1.45 with Slidebook6 software (Zeiss, Intelligent Imaging Innovations, Denver, CO). Z stack images (11-17 stacks along the z axis at 0.5 μm intervals for Rabs/Vps8ap, Vps8ap/Sor4p, Sor4p/Rab7p co-localization analysis; 23-44 and 18-40 stacks along the z axis at 0.25 μm intervals for Rab22Ap and Rab7p particles analysis, respectively) were processed with Huygens Professional software (Scientific Volume Imaging), colored, denoised and adjusted in brightness/contrast with the program Fiji [86]. Images shown are single slices for clarity.

Live cell imaging

Tetrahymena cells expressing Grl3p-GFP, Sor4p-GFP, Igr1p-GFP, mCherry-Rab7p, or mCherry-Rab22Ap were grown overnight to 1-2x10^5cells/ml and transferred to S medium for 2h unless otherwise indicated, prior to imaging. Igr1p-GFP expression was induced with $CdCl_2$ at 30°C for 4h, as described earlier, while mCherry-Rab7p and mCherry-Rab22Ap expression was induced with 1 μg/ml of $CdCl_2$ for 2.5 h. Cells were immobilized in a thin 3% low melting agarose gel pad as described previously [48]. Z stack images (5-10 stacks along the z axis at 0.5-2 μm intervals) and time-lapse videos of cells expressing mCherry-Rab7p, and mCherry-Rab22Ap (20 frames, 0.1ms interval), were collected with a Zeiss LSM 880 Confocal Laser Scanning Microscope, 100X oil with NA = 1.4, with Zen2.1 software (Zeiss, Thornwood, NY). Images and movies were processed with Huygens Professional software (Scientific Volume Imaging), colored, denoised and adjusted in brightness/contrast using Fiji [86]. Images shown are single slices/frames for clarity.

Labeling endocytic and acidic compartments with FM4-64 and LysoTracker

Tetrahymena cells were incubated for 5 min with 5 μM FM4-64, or 7 min with 500 nM LysoTracker (Invitrogen). Cells were washed twice with S-medium, immobilized for live microscopy in 3% low melting agarose gel pads, and imaged within 15-30 min.

Electron microscopy

Cells were grown, starved and prepared for electron microscopy as previously described [48]. Fixation was performed at room temperature with 2.5% glutaraldehyde, 1.5% sucrose, and 2% osmium in 6.7 mM sodium cacodylate buffer.

CLEM imaging

Tetrahymena cells (CU428.1 or SB281) expressing Igr1-GFP were fixed with 2.5% glutaraldehyde for 1h at room temperature and washed 4x with 0.1 M phosphate buffer (PB), pH 7.4, and then incubated with 0.5 μg/ml 4',6-diamidine-2′-phenylindole (DAPI), a specific DNA-staining fluorescence dye, to stain DNA for 10 min at room temperature. After washing with PB once, the cells were embedded in an agarose gel (0.5% low melting temperature agarose) on a glass bottom dish (P35G-1.5-10-C, MatTek, Ashland, MA, USA). 3D images (80 z stacks x 0.2 μm intervals) were obtained using an oil immersion objective lens (PlanApoN60xOSC/NA1.4; Olympus, Tokyo, Japan) on the DeltaVision microscope system (GE Healthcare Life Sciences, USA) and processed by deconvolution using softWoRx software equipped on the microscope system. For EM observation, the same cells in the agarose gel were treated as previously described [103, 104]. In detail, the cells were post-fixed with 1% OsO_4 (Nisshin EM, Tokyo, Japan) in PB for 1h, and then washed briefly 3 times with distilled water. The samples were stained en bloc with 2% uranyl acetate (Wako, Osaka, Japan) for 1h, and washed 3 times with distilled water. Dehydration was performed by treatment with a sequential series of ethanol, 30% for 1 min, 50% for 3 min, 70% for 5 min, 90% for 5 min, 99.5% for 10 min and 3x 100% for 10 min. The sample was then sequentially treated with 10, 30, 50, 70 and 90% (v/v in ethanol) Epon812 (TAAB, Berkshire, UK) for 20 min each, and finally treated 3 times with 100% Epon812 for 2-3h each. After removal of Epon from the dish, a Beem capsule (414-1, Nisshin EM, Tokyo, Japan) filled with 100% Epon was placed on the sample area and incubated for 48h at 60°C to allow the Epon to coagulate. The epoxy block was detached from the glass bottom dish after briefly heating the bottom of the dish. The cells of interest were identified by looking through the binoculars of the microscope equipped with a ultramicrotome (UC6rt, Leica Microsystems, Wetzlar, Germany). The surface region of the epoxy block containing the cells of interest was trimmed and sliced to 80 nm sections with the ultramicrotome. The sections were stained with 4% uranyl acetate (Wako, Tokyo, Japan) for 15 min and a commercial ready-to-use solution of lead citrate (Sigma-Aldrich, St. Louis, USA) for 1 min. Image data were collected by JEM-1400 (JEOL, Tokyo, Japan) with an accelerating voltage of 80 kV. To make a correlation between fluorescence microscope (FM) and electron microscopy (EM) images, the aspect ratio of the fluorescence images corresponding to the EM images was adjusted to 1.00 to 1.23 or to 1.13 for Figure 2I and 2J, respectively, using Powerpoint software. Then, a display mode of FM images was inverted from the negative to the positive one using Photoshop software. Finally, the FM images were overlaid to the EM images using Powerpoint with 50% transparency to generate a single montage image.

Dibucaine assay

Cultures were grown to stationary phase (10^6 cells/ml) in 25 mL SPP for 48 h, and then concentrated into a loose 1.5 mL pellet. Cells were stimulated with 2.5 mM dibucaine, vigorously mixed for 30 s and diluted to 15 mL with 10 mM HEPES, pH 7.5, and 5 mM $CaCl_2$. After gently mixing, the culture was then centrifuged at 1,200 *g* for 2 min, resulting in the formation of a cell pellet/flocculent bilayer.

Immunoprecipitation

The following protocol was used in immunoprecipitation of Vps8ap-GFP, Sor4p-GFP, Vps8ap-mNeon and Sor4p-mNeon, prior to visualization by western blotting. Cells were grown overnight to 1.5-2x10^5 cells/ml. Vps8ap-GFP and Sor4p-GFP were immunoprecipitated with GFP-nAb agarose Spin Kit (Allele Biotechnology Inc., San Diego, CA) from detergent cell lysates, as follows. 400 mL cultures were starved for 1 h in 10 mM Tris, pH 7.4, pelleted and resuspended in lysis buffer [20 mM Tris-HCl pH 7.4, 50 mM NaCl, 1 mM $MgCl_2$, 1 mM DTT, 1 mM EGTA, 0.2% NP-40, 10% glycerol], supplemented with cOmplete EDTA-free protease inhibitor cocktail tablets (Roche). After 45 min at 4°C, lysates were cleared by centrifugation at 30000 rpm (Beckman type 45 Ti rotor) for 1 h. 80 μL of pre-washed GFP-nAb agarose resin were added to the cleared lysates and mixed for 3h at 4°C. The beads were then washed once with wash buffer (10 mM Tris-HCl pH 7.4, 500 mM NaCl), transferred to a spin column and washed five times with wash buffer. GFP-tagged proteins were eluted by adding 500 μL of 0.2 M glycine, pH 2.5. Proteins were precipitated with 10% trichoroacetic acid (TCA) and 0.02% deoxycholate (DOC), and resuspended in 40 μL 100°C SDS-PAGE sample buffer.

Vps8a-mNeon and Sor4p-mNeon were immunoprecipitated in parallel from cell lysates with nProtein A Sepharose 4 Fast Flow resin (GE Healthcare Life Sciences). Sor4p-mNeon expression was induced with 0.5 μg/ml $CdCl_2$ for 3h. Cells expressing Vps8ap-mNeon from the *VPS8A* locus were similarly treated with $CdCl_2$, to avoid differences due to cadmium stress. 200 mL cultures were washed once with 10mM Tris, pH 7.4 and lysed as described earlier. The cleared lysates were mixed with 50 μL nProtein A Sepharose beads, which were pre-conjugated with ~50 μg mouse anti-c-*myc* mAb (9E10) for 2h at 4°C, according to the manufacturer's instructions. The beads were then washed three times with 20 mM Tris-HCl pH8, 1 mM EDTA, 50 mM NaCl, 0.1% NP-40, 1 mM DTT, 10% glycerol supplemented with cOmplete EDTA-free protease inhibitor cocktail tablets (Roche). Proteins were eluted with 400 μL 0.1M glycine pH 2.5, precipitated with 10% TCA and 0.02% deoxycholate, and dissolved in 40 μL 100°C SDS-PAGE sample buffer.

Co-immunoprecipitation

Vps8ap-FF-ZZ fusion protein was immunoprecipitated from detergent lysates of cells that were also transiently expressing either Vps16ap-HA or Vps16bp-HA, using anti-FLAG beads (EZ view Red Anti-FLAG M2 Affinity Gel, Sigma). In brief, 250ml cultures were grown overnight to 1x10^5 cells/ml, then treated with 1 μg/ml of $CdCl_2$ for 2.5h. They were washed once with 10 mM Tris, pH 7.4, pelleted and resuspended for 45min in cold lysis buffer (20 mM Tris-HCl pH 7.4, 50 mM NaCl, 1 mM $MgCl_2$, 1 mM DTT, 1 mM EGTA, 0.2% NP-40, 10% glycerol, 4% BSA), supplemented with protease inhibitor cocktail tablets (Roche). Lysates were cleared by centrifugation at 35000 rpm (Beckman type 45 Ti rotor) for 1.5 h. 75 μL of anti-FLAG beads, pre-incubated with cold lysis buffer for 2h, were added to the cleared lysates and mixed for 2h at 4°C. The beads were then washed five times with 20 mM Tris-HCl pH8, 1 mM EDTA, 1 M NaCl, 0.1% NP-40, 1 mM DTT, 10% glycerol, and resuspended in 100 μL 100°C SDS-PAGE sample buffer. C-myc-Rab7 and c-*myc*-Rab22A fusion proteins were immunoisolated from detergent lysates of cells co- expressing Vps8ap-FF-ZZ, using anti-c-*myc* beads (Pierce Anti-c-Myc Agarose, Thermo Scientific). In brief, 300ml cultures were grown overnight to 2x10^5 cells/ml. They were washed once with 10 mM Tris, pH 7.4, pelleted and treated as described above. 400 μL of anti-c-*myc* beads, pre-incubated with cold lysis buffer for 2h, were added to the cleared lysates and mixed for 2h at 4°C. The beads were then washed five times with 20 mM Tris-HCl pH7.4, 1 mM EDTA, 500mM NaCl, 0.1% NP-40, 1 mM DTT, 10% glycerol, and resuspended in 80 μL 100°C SDS-PAGE sample buffer.

Western blotting

For western blotting of whole cell lysates, 5x10^5 cells from overnight cultures were washed once with 10 mM Tris pH 7.4, resuspended in 500 μL 10 mM Tris, and precipitated with 10% TCA on ice for 30 min. Samples were then centrifuged at 12000 rpm (Eppendorf F-45-30-11 rotor) in an Eppendorf microfuge for 10 min at 4°C, washed once with ice-cold acetone and resuspended in 100 μL 100°C SDS-PAGE sample buffer. Proteins were resolved with the Novex NuPAGE Gel system (4%–20% Tris-Glycine gels, Invitrogen), and transferred to 0.2 μm PVDF membranes (Thermo Scientific). Blots were blocked with 5% dried milk or 3% BSA in 1X TBS-Tween (25 mM Tris, 3 mM KCl, 140 mM NaCl, 0.05% Tween 20, pH 7.4). The rabbit anti-Grl1p serum, the mouse mAb anti-GFP (BioLegend), the mouse mAb anti-c-*myc* (9E10, Sigma), the rabbit anti-FLAG (Sigma), and the mouse mAb anti-HA (HA.11, BioLegend) antibodies, were diluted 1:2000, 1:5000, 1:1000, 1:2000, 1:2000, respectively, in blocking solution. Proteins were visualized with either anti-rabbit IgG (whole molecule)-HPeroxidase (Sigma) or ECL Horseradish Peroxidase-linked anti-mouse (NA931) (GE Healthcare Life Sciences, Little Chalfont, UK) secondary antibody diluted 1:20000, and SuperSignal West Femto Maximum Sensitivity Substrate (Thermo Scientific).

Homology searching and Phylogenetic tree construction

For the comparative genomic detection of VPS8 homologs in the Oligohymenophorea, Vps8 sequences from diverse eukaryotes were used as queries against translated ORF coding sequences from the genomes and transcriptomes of selected ciliate species using the BLAST algorithm. Positive BLAST hits against a Vps8 query were those with an E value of less than 0.05, for which

reciprocal BLAST against the genome containing the query sequence retrieved either the same sequence or an isoform of the sequence with the same E value or lower. To identify a hit as orthologous to the query, we further required that the E value be at least three orders of magnitude lower than the next lowest hit. Hits that were consistent with the first two criteria but did not show clear superiority over other hits were classified as potential hits, which may be either Vps8 or 41, or Vps3 or 39.

Once homologs of HOPS/CORVET had been determined via BLAST, the phylogenetic relationships of the VPS8 homologs within the Oligohymenophorea were determined using both maximum likelihood (via the RAxML algorithm) and Bayesian inference (via the MrBayes algorithm) run using the CIPRES server. Homologs were aligned using MUSCLE and alignments were manually trimmed to retain regions of unambiguous homology. For the RAxML trees, ProtTest was used to select an appropriate rate evolution model. Consensus trees were constructed through manual inspection of both RAxML and MrBayes outputs and determination of corresponding nodes, mapped onto the MRBayes topology. The root of the tree was determined using *Oxytricha trifallax* Vps8 sequences as an outgroup, showing that expansions within the Spirotrichea were lineage specific and the post-Spirotrichea expansions form a single clade with MrBayes/RAxML support values of 1/100.

QUANTIFICATION AND STATISTICAL ANALYSIS

Colocalization analysis

To estimate the extent of colocalization, the Fiji-JACoP plugin was used to calculate Manders' coefficients M1 or M2 [105]. M1 is defined as the ratio of the summed intensities of pixels from the green image for which the intensity in the red channel is above zero to the total intensity in the green channel, and M2 is defined conversely for red. The images were corrected for noise, and the M1 and M2 coefficients were calculated setting the threshold to the estimated value of background. Between 25 and 65 non-overlapping images were analyzed for each sample. In particular, to measure the extent of Vps8ap/Sor4p, and Sor4p/Rab7p co-localization, 100 and 206-213 non-overlapping images were collected, respectively.

Particle analysis

The estimation of the number and size of particles was obtained by using the Fiji tool "Analyze Particles" (http://imagej.nih.gov/ij/). The number of particles was calculated using non-overlapping images, which were corrected for noise and analyzed by setting the threshold to the estimated background value, and then converted to "Mask." The calculation was restricted to different area-based size ranges, selected on the base of the overall population size in both WT and *Δvps8a* cells, including particles between 0.1 and 3 μm^2 for Sor4p-GFP particles, between 0.2 and 3 μm^2 for mCherry-Rab22Ap particles, and between 0.2 and 8 μm^2 for mCherry-Rab7p- particles. The number of particles with a given size is reported as Mean value.